Article

Immunity

Signaling via a CD27-TRAF2-SHP-1 axis during naive T cell activation promotes memory-associated gene regulatory networks

Graphical abstract

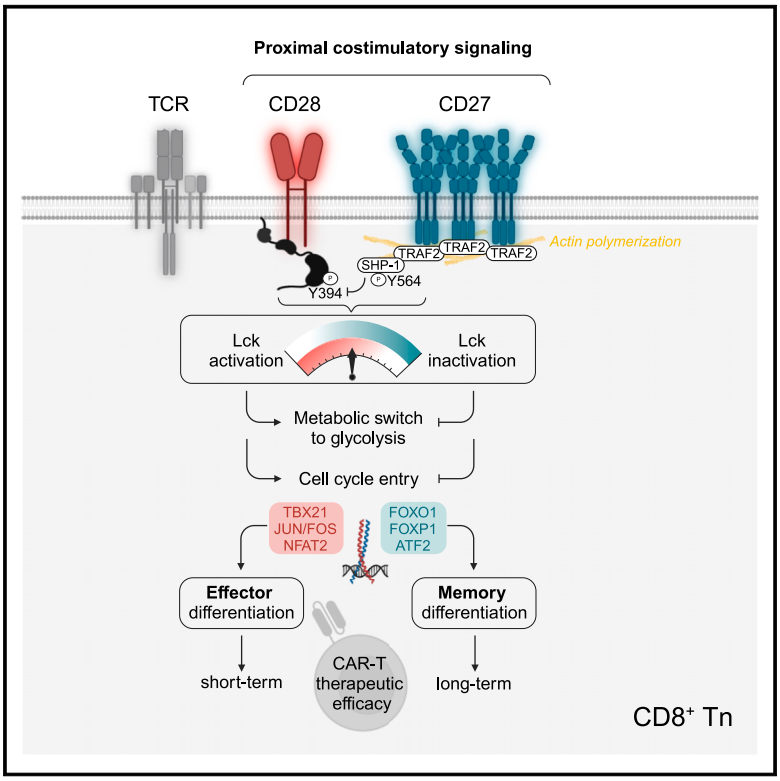

Highlights

- CD27 is rapidly endocytosed in activated naive T cells after binding its ligand CD70
- CD27-TRAF2-SHP-1 modulates Lck phosphorylation in CD28-costimulated naive T cells
- CD27 signaling promotes phenotypic and transcriptional adaptations of T cell memory
- CAR-T cells generated with CD27 costimulation have superior antitumor efficacy

Authors

Carla A. Jaeger-Ruckstuhl, Yun Lo, Elena Fulton, ..., Lucas B. Sullivan, Scott N. Furlan, Stanley R. Riddell

Correspondence

cjaeger@fredhutch.org (C.A.J.-R.), sriddell@fredhutch.org (S.R.R.)

In brief

Interaction of CD27 on naive T cells with CD70 on antigen-presenting cells is necessary for T cell memory fate determination. Jaeger-Ruckstuhl et al. engineer a trimeric CD70-ligand and assess consequences of CD27 ligation on receptor regulation, early proximal signaling, transcriptional and epigenetic states, revealing how modulation of T cell activation by CD27 affects fate commitment and efficacy of T cell immunotherapy.

Jaeger-Ruckstuhl et al., 2024, Immunity *57*, 287–302
February 13, 2024
https://doi.org/10.1016/j.immuni.2024.01.011

CellPress

Immunity

CellPress
OPEN ACCESS

Article

Signaling via a CD27-TRAF2-SHP-1 axis during naive T cell activation promotes memory-associated gene regulatory networks

Carla A. Jaeger-Ruckstuhl,[1,*] Yun Lo,[1] Elena Fulton,[1] Olivia G. Waltner,[1] Tamer B. Shabaneh,[1] Sylvain Simon,[1] Pranav V. Muthuraman,[1] Colin E. Correnti,[1] Oliver J. Newsom,[2] Ian A. Engstrom,[2] Sami B. Kanaan,[1] Shruti S. Bhise,[1] Jobelle M.C. Peralta,[1] Raymond Ruff,[1,3] Jason P. Price,[1,3] Sylvia M. Stull,[1] Andrew R. Stevens,[1] Grace Bugos,[1] Mitchell G. Kluesner,[2] Valentin Voillet,[4] Vishaka Muhunthan,[1] Fionnuala Morrish,[1] James M. Olson,[1,3] Raphaël Gottardo,[4,5,6] Jay F. Sarthy,[3,7] Steven Henikoff,[7,8] Lucas B. Sullivan,[2] Scott N. Furlan,[1,3] and Stanley R. Riddell[1,9,10,*]

[1]Translational Sciences and Therapeutics Division, Fred Hutchinson Cancer Center, Seattle, WA 98109, USA
[2]Human Biology Division, Fred Hutchinson Cancer Center, Seattle, WA 98109, USA
[3]Seattle Children's Hospital, Seattle, WA 98105, USA
[4]Vaccine and Infectious Disease Division, Fred Hutchinson Cancer Center, Seattle, WA 98109, USA
[5]Department of Statistics, University of Washington, Seattle, WA 98195, USA
[6]Swiss Institute of Bioinformatics, University of Lausanne and Lausanne University Hospital, Lausanne 1011, Switzerland
[7]Basic Science Division, Fred Hutchinson Cancer Center, Seattle, WA 98109, USA
[8]Howard Hughes Medical Institute, Seattle, WA 98195, USA
[9]Department of Medicine, University of Washington, Seattle, WA 98195, USA
[10]Lead contact
*Correspondence: cjaeger@fredhutch.org (C.A.J.-R.), sriddell@fredhutch.org (S.R.R.)
https://doi.org/10.1016/j.immuni.2024.01.011

SUMMARY

The interaction of the tumor necrosis factor receptor (TNFR) family member CD27 on naive CD8$^+$ T (Tn) cells with homotrimeric CD70 on antigen-presenting cells (APCs) is necessary for T cell memory fate determination. Here, we examined CD27 signaling during Tn cell activation and differentiation. In conjunction with T cell receptor (TCR) stimulation, ligation of CD27 by a synthetic trimeric CD70 ligand triggered CD27 internalization and degradation, suggesting active regulation of this signaling axis. Internalized CD27 recruited the signaling adaptor TRAF2 and the phosphatase SHP-1, thereby modulating TCR and CD28 signals. CD27-mediated modulation of TCR signals promoted transcription factor circuits that induced memory rather than effector associated gene programs, which are induced by CD28 costimulation. CD27-costimulated chimeric antigen receptor (CAR)-engineered T cells exhibited improved tumor control compared with CD28-costimulated CAR-T cells. Thus, CD27 signaling during Tn cell activation promotes memory properties with relevance to T cell immunotherapy.

INTRODUCTION

The expression of the tumor necrosis factor receptor (TNFR) family member CD27 is confined to the earliest hematopoietic cell progenitors and to cells of the lymphoid cell lineage.[1–3] CD27 is highly expressed by naive CD8$^+$ T (Tn) cells, maintained in stem cell (Tscm) and central memory (Tcm) cells, and expressed at lower levels in only a subset of effector memory (Tem) and terminal effector (Teff) cells.[4,5] During antigen priming of Tn cells, the interaction of CD27 with its homotrimeric ligand CD70, which is transiently induced on antigen-presenting cells (APCs), is necessary for T cell memory fate determination.[6–9] Overexpression of CD27 in HEK 293 cells induces pro-survival signals via nuclear factor κB (NF-κB)-inducing kinase (NIK), stress-activated protein kinase (SAPK), and c-JUN N-terminal kinase (JNK).[10] In murine T cells, TNFR-associated factor 2 (TRAF2)- and Nck-interacting kinase (TNIK) act downstream of the CD27 receptor to promote Wnt pathway activation.[11] These findings identify important CD27 functions but do not fully explain how CD27 might cooperate with the T cell receptor (TCR) and CD28 signaling to affect T cell fate.

The potential to enrich and preserve memory T cell states during *in vitro* T cell expansion is of interest for adoptive T cell therapy.[12] T cells engineered to express chimeric antigen receptors (CARs) that target tumor-associated antigens exhibit potent activity in hematologic malignancies.[13] Preparation of CAR-T cells for adoptive transfer involves activation with αCD3 and αCD28 antibodies to facilitate gene insertion and increase cell numbers but leads to progressive T cell differentiation that may compromise long-term efficacy. Higher numbers of CD27$^+$ cells in the

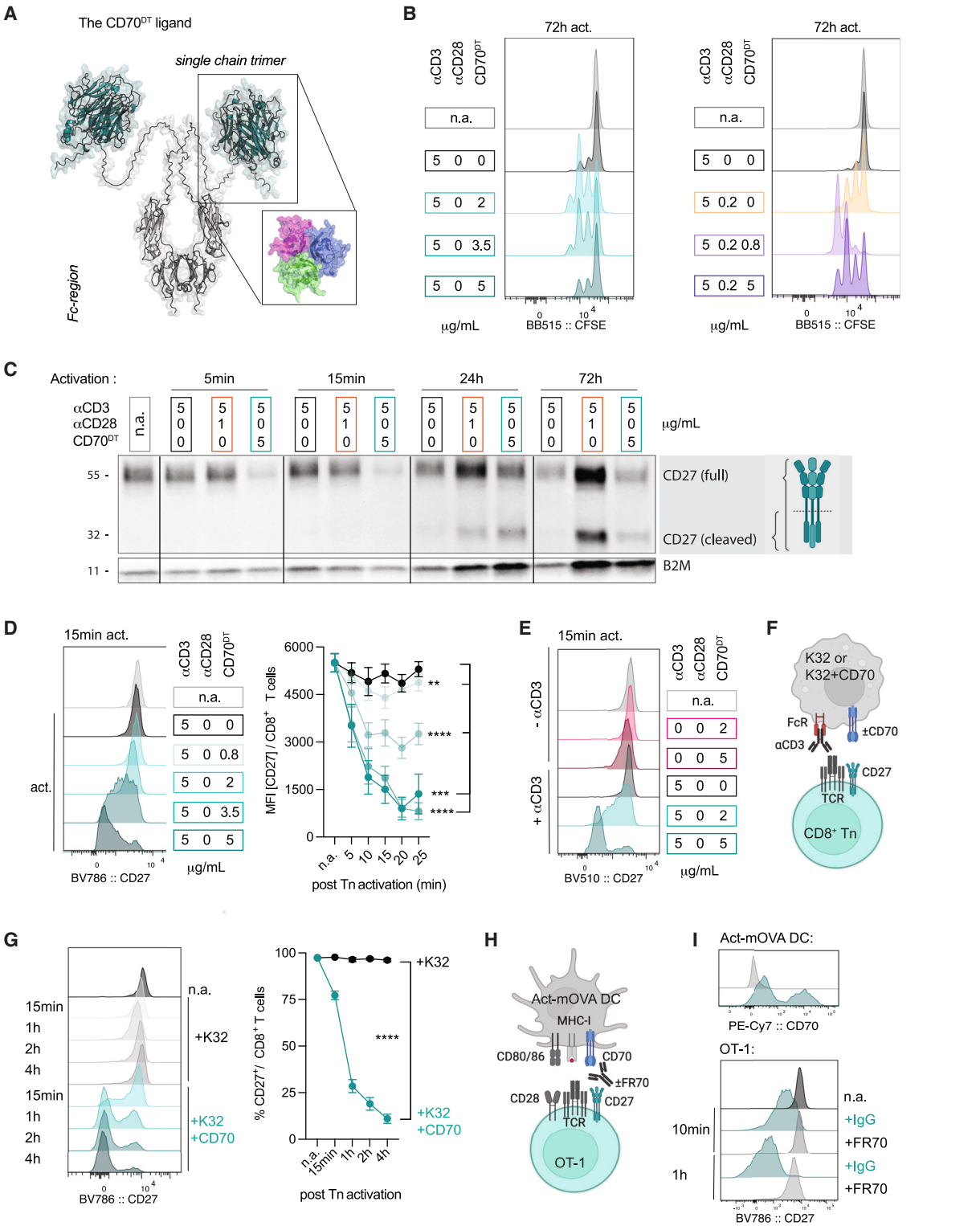

Figure 1. CD70 ligand binding induces rapid surface CD27 receptor down-modulation

(A) Model of the Fc-fused dimer of assembled CD70 single-chain trimers.

(B) Representative histograms of a CFSE-dilution assay of non-activated (n.a.) or 72-h-activated cells following stimulation with (left) αCD3+CD70^{DT} or (right) combinations of αCD3+αCD28+CD70^{DT} (µg/mL).

(C) Western blot of lysates from Tn cells that were n.a. or activated with the indicated concentrations of αCD3,αCD28, andCD70^{DT} for 5 min, 15 min, 24 h, and 72 h. Blots for CD27 (full-length 55 kDa and cleaved 28–32 kDa) and beta 2 microglobulin (B2M) loading control are shown for each stimulation condition.

(legend continued on next page)

starting T cell population and CAR-T products containing gene expression signatures of less differentiated cells provide for more durable antitumor responses.[14,15] Given the role of CD27 in promoting T cell memory *in vivo*, we sought to understand the regulation and function of CD27 after ligation with CD70 *in vitro*. To engage CD27 as a trimer, we designed functional CD70 trimeric ligands.[16] We found that CD27 ligation by plate-coated CD70 in conjunction with TCR stimulation provided by αCD3 monoclonal antibody (mAb) promoted rapid internalization of CD27 in a dose-dependent manner. This effect preceded CD27 cleavage and was observed in antigen-specific $CD8^+$ T cells interacting with APCs that expressed physiologic levels of CD70. CD27 costimulation improved proliferation of Tn cells activated with αCD3 mAb alone, but when strongly engaged, antagonized CD28 signaling. This effect was mediated by co-recruitment of TRAF2 and the phosphatase SHP-1, and de-phosphorylation of the tyrosine kinase Lck. Compared with CD28 costimulation of αCD3-activated Tn cells, costimulation via CD27 transiently restrained cell cycle entry and induced a distinct metabolic, transcriptional and epigenetic state. Consequently, CD27-costimulated CAR-T cells exhibited a phenotype similar to memory T cells and had improved therapeutic activity in models of chronic antigen stimulation and cancer.

RESULTS

Binding of CD27 by CD70 induces receptor endocytosis

To investigate the consequences of CD27 ligation, we designed an Fc-fused dimer of single-chain CD70 trimers ($CD70^{DT}$) that provides costimulation to T cells activated with αCD3 mAb or with a combination of αCD3 and αCD28 mAb (Figures 1A, 1B, and S1A). $CD70^{DT}$ alone did not induce CD69 expression or cell division as measured by CFSE dye dilution, indicating dependence on αCD3 engagement for costimulatory effects (Figure S1B). To determine how ligand engagement might affect CD27 expression, we used western blot with an antibody specific to the CD27 endodomain to evaluate total CD27 protein levels in lysates from Tn cells stimulated with αCD3 mAb alone, with αCD3+αCD28 mAb, or with αCD3+$CD70^{DT}$. Consistent with previous reports that CD27 undergoes cleavage in activated T cells,[17,18] a 28-kDa cleavage product was detected in all stimulated conditions at 24 h and was prominent at 72 h (Figure 1C). As early as 5 min after Tn cell activation, we observed a marked reduction of the intact 55-kDa CD27 single chain that was dependent on ligation by CD70 and occurred before the 28-kDa cleavage product was detected (Figure 1C). Assessment of cell surface CD27 by flow cytometry revealed a rapid dose-dependent reduction after ligation with $CD70^{DT}$ in αCD3 and αCD3+αCD28-stimulated T cells but minimal loss with $CD70^{DT}$ ligation alone (Figures 1D, 1E, and S1C). The rapid decline in cell surface CD27 after αCD3+$CD70^{DT}$ stimulation was not associated with differences in CD27 mRNA levels, prevented by inhibiting matrix metalloproteinases responsible for cleavage, or due to competition for αCD27 antibody-binding epitopes by $CD70^{DT}$ (Figures S1D–S1F). CD27 internalization occurred in all $CD8^+$ T cell subsets (Tn, Tcm, Tem, $CD45RA^+$ Tem [Temra]) activated with αCD3+$CD70^{DT}$ (Figure S1G).

To determine whether CD27 internalization was also observed upon interaction with CD70 expressing APCs, we co-cultured Tn cells with K562-derived APCs that stably expressed the Fcγ receptor CD32 (K32)[19] and were transduced with a vector encoding CD70 (Figures 1F and S1H). CD27 internalization was observed in co-cultures with CD70-transgene expressing K32 cells presenting αCD3 mAb, but not with K32 cells that did not express CD70 (Figure 1G). Rapid CD27 receptor internalization was also observed in murine OT-1 T cells co-cultured with matured bone marrow (BM) derived ovalbumin transgenic dendritic cells (DCs) that expressed endogenous levels of CD70 and was inhibited by the addition of a CD70 blocking antibody to prevent CD27 binding (Figures 1H and 1I).

We next sought to define the mechanism for the rapid loss of cell surface CD27 after ligand binding. TNFR1 is internalized by clathrin-mediated endocytosis (CME) upon TNF binding suggesting CD27 may undergo similar regulation.[20,21] CME involves clathrin, dynamin, actin, and endophilin for the initiation of membrane pit formation and subsequent endocytic vesicle scission.[22] We therefore measured CD27 surface expression on αCD3+$CD70^{DT}$-activated Tn cells in the presence or absence of clathrin-heavy-chain inhibitor (ES9–17), dynamin-related protein inhibitors (Mdivi-1, Dynasore, and Dyngo-4a) or combinations thereof (Figure 2A). CD27 surface expression was substantially increased in the presence of CME inhibitors in both the plate-coated and K32 APC activation systems, supporting CME as the mechanism for rapid CD27 internalization (Figures 2B, S2A, and S2B). Inhibitors of autophagy initiation (ULK-101) and proteasomal degradation (Lactacystin) also partially rescued total cellular CD27 levels providing evidence for lysosomal and proteasomal degradation of internalized CD27 (Figure 2C). Levels of cell surface CD27 were gradually restored over 7 days in culture (Figure S2C). These data identify a mechanism by which CD27 surface expression on activated Tn cells is regulated by CD70 binding through rapid ligand-induced CME followed by intracellular receptor degradation and re-expression.

A CD27-TRAF2-SHP-1 axis regulates Lck and downstream signaling induced by TCR and CD28 ligation

CD27 propagates signals via association with TRAFs.[23] To determine whether TRAF2 was recruited during CD27 receptor

(D) (Left) Representative histogram and (right) quantification of mean fluorescent intensity (MFI) of CD27 surface expression on n.a. and activated Tn cells (n = 4 donors).
(E) Representative histogram showing down-modulation of CD27 surface expression induced by $CD70^{DT}$ requires αCD3 stimulation.
(F) Illustration of K32 APC and T cell activation.
(G) (Left) Representative histogram and (right) quantification of percent (%) CD27 surface expression on Tn cells co-cultured (1:1) with αCD3-coated (5 μg/mL) K32 or CD70-transgene-expressing K32 cells (n = 3 donors).
(H) Illustration of BM-derived Ova-presenting DC and OT1 T cell activation.
(I) Representative histogram showing CD27 surface expression on murine OT-1 $CD8^+$ Tn cells co-cultured (2:1) with activated murine BM-derived OVA-presenting DCs in the presence of IgG or αCD70-blocking antibody (FR70). Representative experiment is shown. Data are shown as mean ± SEM and analyzed by one-way ANOVA (D and G). *$p < 0.05$, **$p < 0.01$, ***$p < 0.005$, ****$p < 0.001$. Illustrations (C, F, and H) created using BioRender. See also Figure S1.

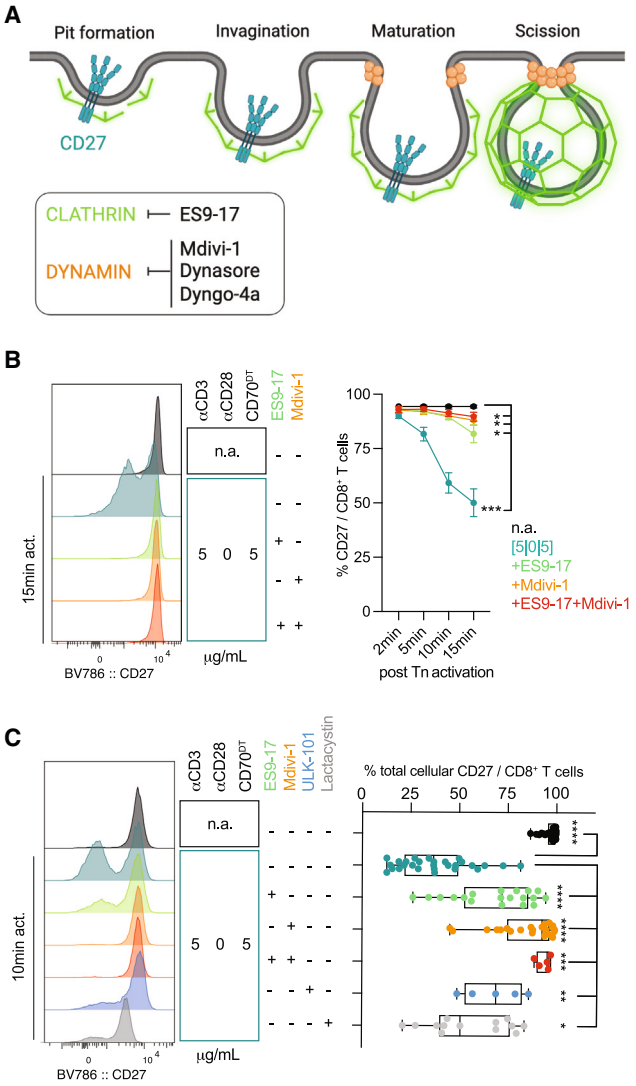

Figure 2. CD27 surface expression is regulated by clathrin-mediated endocytosis

(A) Illustration of clathrin-mediated CD27 receptor endocytosis (CME).

(B) (Left) Representative histogram and (right) quantification of percent (%) CD27 surface expression of non-activated (n.a.) and αCD3+CD70^{DT}-activated (2–15 min) Tn cells treated with ±CME inhibitors (CMEi) ES9-17 (100 µM), Mdivi-1 (50 µM), or a combination of both (right: n = 5 donors).

(C) (Left) Representative histogram of fixed and permeabilized Tn cells and (right) quantification of total cellular CD27 in n.a. or 10 min-activated Tn cells treated with ±CMEi, autophagy inhibitor (ULK-101; 5 µM), or proteasome inhibitor (lactacystin; 20 µM) (n = 5–28 donors). Data are shown as mean ± SEM and analyzed by one-way ANOVA (B) or paired two-tailed Student's t test (C). *p < 0.05, **p < 0.01, ***p < 0.005, ****p < 0.001. Illustration (A) created using BioRender. See also Figure S2.

internalization, we immunoprecipitated TRAF2 in lysates of non-activated or αCD3-stimulated Tn cells in the presence of various doses of αCD28 mAb or CD70^{DT} and examined its association with CD27 by western blot. Whereas CD70^{DT} binding increased TRAF2 association with CD27 in a dose-dependent manner, neither αCD3 alone nor αCD3+αCD28 stimulation promoted its association with CD27 (Figures 3A and S3A). The addition of actin polymerization inhibitor latrunculin A (LatA) prevented CD27 endocytosis and reduced TRAF2 association with CD27 in Tn cells that were stimulated with high dose of CD70^{DT} (Figures 3B and S3B).

Irrespective of the T cell activation state, we found that TRAF2 interacted with SHP-1 but not SHP-2 (Figures 3C and S3C). This led us to hypothesize that CD27 engagement might alter SHP-1 activity. We therefore assessed SHP-1 phosphorylation at activating (Y536 and Y564) and inactivating (S591) residues in unstimulated and 10 min-stimulated Tn cells. No CD27 signaling-induced changes in phosphorylation were observed at residues SHP-1^{Y536} and SHP-1^{S591}, however SHP-1^{Y564} phosphorylation was significantly increased when CD27 was ligated in Tn cells stimulated with αCD3+αCD28 (Figure S3D). Although SHP-1^{Y564} phosphorylation was only minimally increased with αCD3+CD70^{DT} stimulation (Figure 3D), the total cellular amount of THEMIS, a negative regulator of SHP-1[24], was reduced in Tn cells activated with αCD3+CD70^{DT} and αCD3+αCD28+CD70^{DT} (Figure S3E). This suggests that CD27 ligation acts to induce SHP-1 activity, most notably in Tn cells activated with αCD3+αCD28.

We then asked whether CD27-induced changes in SHP-1 might regulate phosphorylation of the SHP-1 substrate Lck, which is crucial for T cell activation.[25] We first assessed whether SHP-1 interacted with Lck by immunoprecipitating SHP-1 from non-activated and 10 min-stimulated Tn cells. SHP-1 co-immunoprecipitated with Lck in all αCD3-activated conditions, independent of SHP-1 phosphorylation state or whether CD28 or CD27 costimulation was provided (Figure 3E). When combined with αCD3+αCD28 activation, CD27 ligation resulted in de-phosphorylation of activating Lck^{Y394} but not inhibitory Lck^{Y505} residues as measured by immunoblot of whole-cell lysates. Stimulation with αCD3+CD70^{DT} had only a minimal effect on Lck^{Y394} (Figure 3F). The addition of an IgG1-Fc control at the same concentration as CD70^{DT} did not result in de-phosphorylation of Lck^{Y394}, demonstrating the requirement for CD27 engagement via its ligand CD70 to modulate Lck (Figure S3F). Lck^{Y394} was also de-phosphorylated when CD70^{DT} was used in the presence of higher αCD28 mAb doses (Figure S3G), suggesting that the recruitment of TRAF2-SHP-1 modulates the sustained activity of Lck mediated by CD28 signaling of various strengths.[26] Small molecule inhibition of SHP-1 prevented de-phosphorylation of Lck^{Y394} in αCD3+αCD28+CD70^{DT}-activated Tn cells (Figure 3G). Collectively, these data show that CD27 ligation results in assembly of a CD27-TRAF2-SHP-1 complex and promotes SHP-1 phosphatase-induced modulation of Lck activity in Tn cells activated through the TCR and CD28.

Lck activity contributes to the magnitude of the extracellular signal-regulated kinase 1/2 (ERK1/2)[27] and phosphatidylinositol 3-kinase (PI3K)[28] response leading us to speculate that CD27-TRAF2-SHP-1 modulation of Lck might affect ERK1/2 and RAC (Rho family)-alpha serine/threonine-protein kinase 1 (AKT) signaling. αCD28 activation enhanced ERK1/2 and AKT phosphorylation over αCD3 activation alone in a dose-dependent manner. Increasing doses of CD70^{DT} combined with αCD3 resulted in a minor increase in ERK1/2 phosphorylation that was significant only at the highest dose of CD70^{DT}, and no increase in AKT phosphorylation was observed (Figures 3H and S3H). When added to αCD3+αCD28, CD70^{DT} reduced phosphorylation of ERK1/2 and AKT significantly compared with

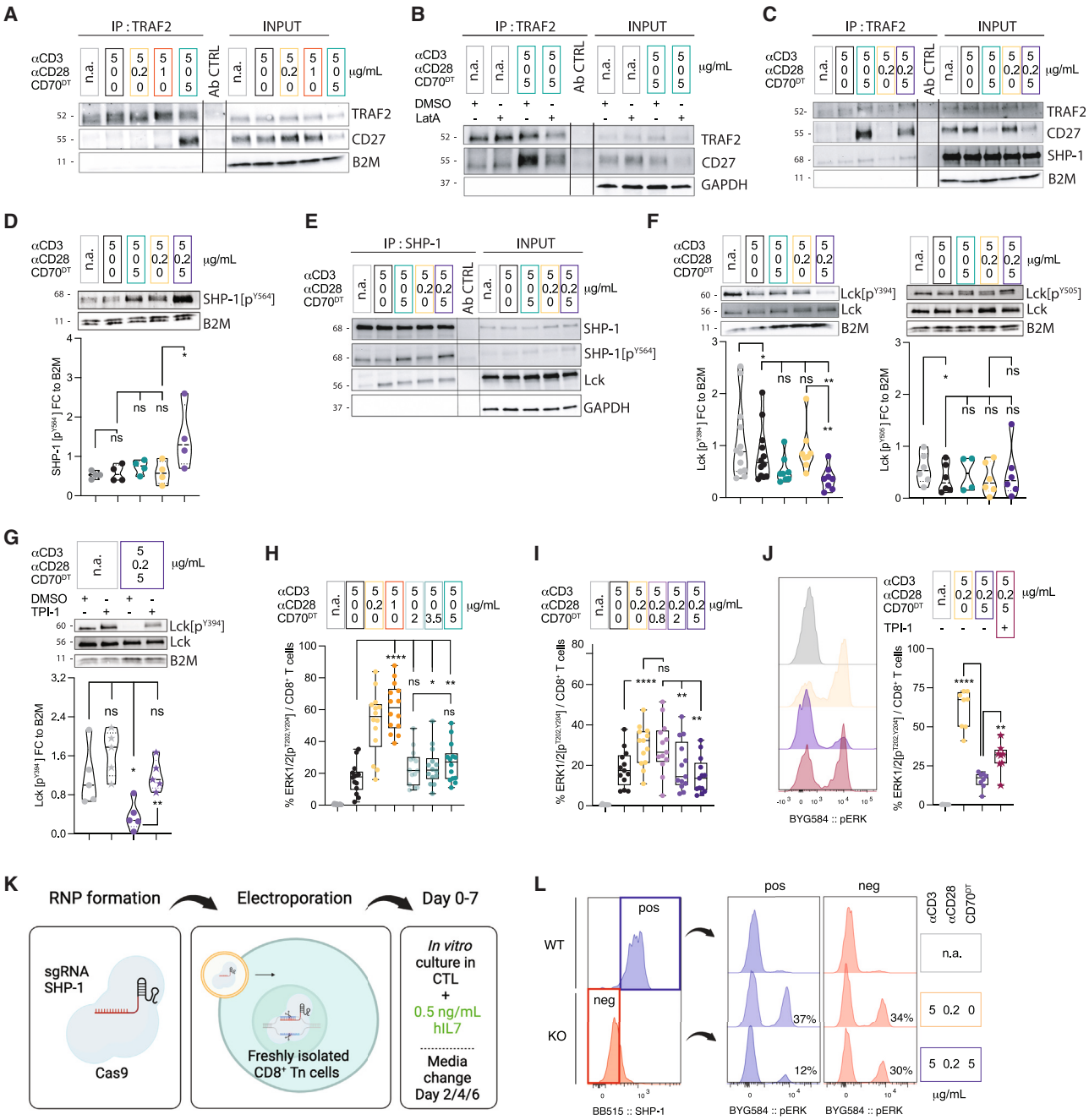

Figure 3. CD27-TRAF2-SHP-1 modulates Lck and downstream signaling induced by αCD3+αCD28

(A) TRAF2 immunoprecipitation of lysates from non-activated (n.a.) and 10 min-activated Tn cells at indicated doses of αCD3, αCD28, and $CD70^{DT}$. Immunoblots for TRAF2, CD27, and B2M are shown.

(B) TRAF2 immunoprecipitation of lysates from n.a. and Tn cells activated for 10 min under the indicated conditions and treated with latrunculin A (LatA, 0.05 µM) or DMSO. Immunoblots for TRAF2, CD27, and GAPDH are shown (1 representative donor of n = 3).

(C) TRAF2 immunoprecipitation of lysates from n.a. and Tn cells activated for 10 min under the indicated conditions. Immunoblots for TRAF2, CD27, SHP-1, and B2M are shown (n = 1).

(D) Representative immunoblots of lysates from n.a. and Tn cells activated for 10 min under the indicated conditions for phospho-SHP-1(Y564) and B2M. Fold-change of band intensity over B2M loading control was calculated (n = 4 donors).

(E) SHP-1 immunoprecipitation of lysates from n.a. and 10 min-activated Tn cells. Immunoblots for SHP-1, phospho-SHP-1(Y564), Lck, and GAPDH are shown (1 representative donor of n = 2).

(F) Representative immunoblots of lysates from n.a. and 10 min-activated Tn cells for Lck, phospho-Lck (Y394 and Y505), and B2M. Fold-change of band intensity over B2M loading control was calculated (n = 8–12 donors for Y394 and n = 4–6 donors for Y505).

(legend continued on next page)

αCD3+αCD28 alone (Figures 3I and S3I). The CD70-mediated modulation of ERK1/2 phosphorylation was also observed using the K32 cell-based co-culture model (Figure S3J). We evaluated ERK1/2 phosphorylation over a range of plate-coated αCD3, αCD28, and $CD70^{DT}$ concentrations and found that ERK1/2 was only modulated at higher $CD70^{DT}$ doses that induced CD27 internalization (Figures 1D, S1C, and S3K). The reduction in ERK1/2 phosphorylation by $CD70^{DT}$ was partially prevented by addition of the SHP-1 inhibitor, further linking this effect of CD27 ligation to the TRAF2-SHP-1-Lck signaling axis (Figure 3J). Because small molecule inhibitors may have non-specific effects, we sought further evidence for the involvement of SHP-1 activity downstream of CD27-TRAF2 in regulating ERK1/2 phosphorylation. We therefore generated a SHP-1 gene deletion in resting Tn cells using CRISPR-Cas9-based editing (Figure 3K). Under conditions that favor the maintenance of a $CD45RA^{+}CD62L^{+}CCR7^{+}$ Tn cell phenotype, we achieved a SHP-1 gene deletion efficiency of up to 88 % after 7–8 days in culture, compared with control Tn cells cultured under identical conditions (Figures S3L and S3M). Analysis of ERK1/2 phosphorylation after activation of SHP-1 wild-type (WT) and SHP-1-deleted (knockout [KO]) Tn cells demonstrated that SHP-1 was required for the modulatory effect on ERK1/2 phosphorylation mediated by CD27 costimulation (Figure 3L).

We next evaluated whether CD27 receptor endocytosis was required for the modulation of Lck and ERK1/2 phosphorylation by activating Tn cells in the presence or absence of LatA. Inhibition of CME using LatA not only prevented CD27 receptor internalization (Figure S3B) but also de-phosphorylation of Lck and reduction in ERK1/2 phosphorylation (Figures S3N and S3O). Collectively, these data show that CD28 signaling is modulated by CD27 ligation and CME through SHP-1 phosphatase-mediated de-phosphorylation of Lck and reduction in downstream ERK1/2 and AKT signaling.

CD27 costimulation delays cell cycle entry and promotes a memory phenotype

The strength of TCR and costimulatory signaling are determinants of cell proliferation rate, cell differentiation, and metabolic adaptation.[29] As observed in Figure 1B, the addition of high $CD70^{DT}$ doses to αCD3-activated Tn cells enhanced cell proliferation over αCD3 alone, indicating that CD27 costimulation has effects on Tn cells that are independent of its modulatory role on CD28 signaling. To measure how CD27 engagement affects cell division, we assessed cell cycle states at 48 and 96 h after αCD3 stimulation alone or combined with CD27 or CD28 costimulation. In addition to plate-coated reagents, we included αCD3+αCD28 beads that are used to propagate T cells for adoptive T cell therapy. αCD3+$CD70^{DT}$ stimulation resulted in slightly more T cells in S and G2+M phase at 48 h post Tn cell activation compared to αCD3 activation alone. However, unlike with αCD3 activation alone, the delay in cell cycle entry observed in αCD3+$CD70^{DT}$-activated Tn cells was only transient, and comparable to Tn cells activated with αCD3 and a lower dose of αCD28. αCD3+αCD28 bead activation and αCD3 stimulation combined with the higher dose of plated-coated αCD28 mAb strongly promoted cell cycle entry (Figure 4A). Assessment of cell counts after 9 days of culture revealed that stimulation with αCD3+$CD70^{DT}$ resulted in a moderate T cell expansion, which was inferior to αCD3+αCD28 beads and strong αCD3+αCD28 activation, but superior to weak αCD3+αCD28 activation or αCD3 activation alone (Figure 4B).

To examine how CD27 signaling might affect cell differentiation at the end of the 9 day expansion, we assessed expression of T cell factor 1 (TCF1), a transcription factor (TF) associated with T cell stemness.[30] αCD3+$CD70^{DT}$ stimulation of Tn cells resulted in a higher fraction of $TCF1^{+}CD27^{+}$ expressing T cells than observed with all αCD3+αCD28 conditions or with αCD3 stimulation alone (Figure 4C). Only CD27 and strong CD28 costimulation resulted in a high expression of CD127 and CCR7 (Figure 4D) whereas T cells stimulated with αCD3 alone or with weak CD28 costimulation expressed these markers at lower levels, despite their low expansion more similar to αCD3+$CD70^{DT}$ activation. Compared with αCD3+αCD28 bead-activated Tn cells, αCD3+$CD70^{DT}$-activated Tn cells maintained a higher fraction of CD45RA positive and CD45RO negative cells, consistent with enrichment of T cells with a Tscm phenotype (Figure 4E). αCD3+$CD70^{DT}$-activated Tn cells also exhibited a higher frequency of Interleukin-2 (IL-2)-positive cells and lower frequency of interferon gamma (IFNγ)-positive cells after PMA and ionomycin restimulationat the end of a 9-day culture (Figure S4A). Thus, CD27 costimulation alone promotes moderate cell proliferation and preserves a memory cell surface phenotype.

T cell differentiation state and cellular metabolism are closely linked.[31] Extensive glycolysis is associated with adoption of an effector rather than memory fate[32] and coincides with activation-induced mitochondrial remodeling.[33] To evaluate how CD27 costimulation affected glucose consumption, we measured depletion of [^{13}C] glucose in the culture supernatants after stimulation of Tn cells with αCD3+$CD70^{DT}$ compared with αCD3 or αCD3+αCD28 beads. We observed increased glucose depletion upon αCD3 activation that was greater when CD27 or CD28 costimulation was provided. At 5 h post Tn cell activation, the rate of glucose consumption in CD27-costimulated Tn cells slowed compared with CD28-costimulated Tn cells (Figure 4F). The lower glycolytic state

(G) Immunoblots of lysates from n.a. and 10 min-activated Tn cells treated with SHP-1 inhibitor (TPI-1, 0.4 μM) or DMSO for total Lck, phospho-Lck(Y394), and B2M. Fold-change of band intensity over B2M loading control was calculated (n = 5 donors).
(H and I) Frequency of phospho-ERK1/2 (T202, Y204) positive T cells in n.a. and 15 min-activated Tn cells assessed by phospho-flow (H: n = 14 donors; I: n = 13 donors).
(J) (Left) Representative histogram and (right) quantification of phospho-ERK1/2 (T202, Y204) in n.a. and 15 min-activated Tn cells treated with DMSO or TPI-1 (0.4 μM) by phospho-flow (n = 8 donors).
(K) Illustration of CRISPR-Cas9-based SHP-1 knockout in human Tn cells and culture conditions.
(L) Flow-cytometry-based assessment of (left) SHP-1 expression in wild-type (WT, blue) or SHP-1 deficient (KO, red) Tn cells and (right) frequency of phospho-ERK1/2 (T202, Y204) positive T cells in n.a. and WT and KO Tn cells activated for 15 min under the indicated conditions (1 representative donor of n = 2). All data are shown as mean ± SEM and were analyzed by paired two-tailed Student's t test (D and F–J). *p < 0.05, **p < 0.01, ***p < 0.005, ****p < 0.001. Illustration (K) created using BioRender. See also Figure S3.

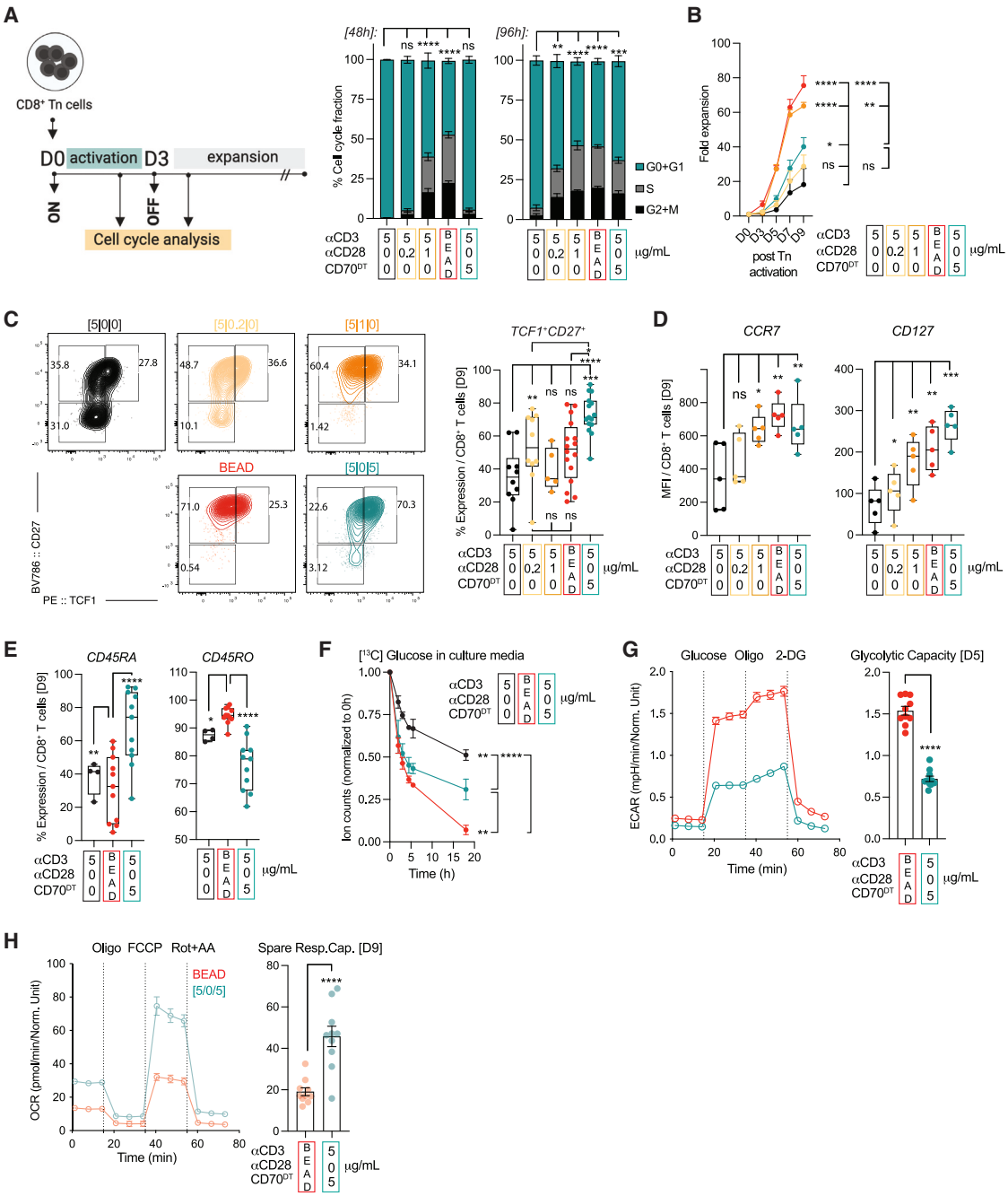

Figure 4. CD27 costimulation promotes memory characteristics

Tn cells are activated under various conditions of plate-bound αCD3,αCD3+αCD28, or αCD3+CD70^{DT}(µg/mL) or αCD3+αCD28 beads (at 3:1 bead:cell ratio) for 72 h and expanded for 9 days.

(A) Cell cycle analysis was performed at 48 and 96 h using 7-AAD nucleic acid stain to determine the fraction of cells in G0 + G1, S, and G2 + M (n = 3–10 donors).

(B) Fold expansion over input of activated Tn cells at respective time points (n = 3–10 donors).

(C) (Left) Representative contour plots showing CD27 and TCF1 expression in Tn cells 9 days after stimulation and (right) quantified fraction of CD27^{+}TCF1^{+} cells (n = 5–10 donors, 2 independent experiments).

(D) Mean Fluorescent Intensity (MFI) of CD127 and CCR7 surface expression 9 days after stimulation (n = 5 donors).

(E) Percent expression of CD45RA and CD45RO on Tn cells expanded for 9 days is shown (n = 4–11 donor of 3 independent experiments).

(F) [^{13}C] glucose uptake from media by Tn cells at various time points after stimulation (n = 3 donors). Ion counts normalized to time point 0 h.

(G) Seahorse-based glucose stress test (left) assessing changes in extracellular acidification (ECAR) and (right) measuring glycolytic capacity of Tn cells 5 days after stimulation (1 donor à 10 replicate wells). Glucose, oligomycin (oligo) and 2-deoxy-D-glucose (2-DG) were added as indicated.

(legend continued on next page)

after αCD3+CD70^{DT} activation was maintained over 5 days of culture as assessed by reduced extracellular acidification rate compared with αCD3+αCD28 bead-activated Tn cells (Figure 4G). In order to address how the observed differences in expansion and effector glycolytic metabolism affected the mitochondrial compartment, we assessed mitochondrial mass using MitoTracker^{green}. The mitochondrial mass of αCD3+CD70^{DT}-activated Tn cells was significantly lower compared with αCD3+αCD28 bead-activated Tn cells at the end of a 9-day culture (Figure S4B). Although αCD3+CD70^{DT}-activated Tn cells harbored a reduced mitochondrial mass, these cells possessed a higher basal oxygen consumption rate and improved spare respiratory capacity compared with αCD3+αCD28 bead-activated Tn cells (Figures 4H and S4C). Taken together, our data show that CD27 costimulation transiently delays cell cycle entry and promotes the acquisition of memory cell surface phenotype, functional, and metabolic properties, independent of its modulatory effect on CD28.

CD27 costimulation induces distinct gene regulatory networks

To better understand differences in the transcriptional and epigenetic responses induced by CD27 or CD28 costimulation, we performed multi-ome single-cell sequencing of Tn cells before and 24 h post stimulation with αCD3+CD70^{DT} or αCD3+αCD28, a time point when T cells had not yet undergone their first cell division. Dimensionality reduction of transcriptomic data identified an intermediate cell population emerging from the naive cluster and bifurcating into two major branches delineated by CD28 or CD27 costimulation. The CD28 branch was further divided into subclusters discriminated by high and low *IL2* transcript levels, whereas the CD27 branch was subclustered by differential expression of effector differentiation repressor Helios encoded by IKAROS family zinc-finger 2 (*IKZF2*)[34] (Figure 5A). Differential gene expression analysis revealed high transcript levels of the regulatory TFs forkhead box (FOX) protein P1 (*FOXP1*),[35,36] stemness-associated TF *TCF7*,[37] inhibitor of glycolysis thioredoxin-interacting protein (*TXNIP*)[38] and epigenetic repressor metastasis-associated lung adenocarcinoma transcript 1 (*MALAT1*)[39] in resting Tn cells. Tn cells that were αCD3+CD70^{DT}-activated for 24 h maintained high transcript levels of these Tn cell-associated genes, which were strongly decreased in response to CD28 costimulation. Genes that were induced in response to CD27 costimulation included the NF-κB cofactor[40,41] and quiescence regulator[42] signal transducer and activator of transcription 1 (*STAT1*), protein arginine methyltransferase 2 (*PRMT2*), transcriptional repressor zinc-finger and BTB-domain-containing 20 (*ZBTB20*), costimulatory receptor *CD96*,[43] nuclear TCF1-cofactor lymphoid-enhancer-binding factor 1 (*LEF1*) as well as memory-associated surface markers *SELL* and *CCR7*. Unique CD28 costimulation-induced genes were associated with cell division (cyclin D2 [*CCND2*], tubulin beta class I [*TUBB*], marker of proliferation Ki-67 [*MKI67*]), effector metabolism (glyceraldehyde-3-phosphate dehydrogenase [*GAPDH*], Enolase 1 [*ENO1*], fatty-acid-binding protein 5 [*FABP5*], *MYC*), stress response (heat shock protein 90 [*HSP90*]), and IL2 sensitivity (*IL2*, IL2 receptor alpha [*IL2RA*]) (Figures 5B and S5A).

Assay for transposase-accessible chromatin (ATAC)-seq analysis revealed that the transition from resting Tn cells to 24 h αCD3+αCD28-activated Tn cells induced extensive remodeling of the DNA architecture, broadly enhancing its accessibility. The transition from resting Tn cells to 24 h αCD3+CD70^{DT}-activated Tn cells resulted only in a modest increase in DNA accessibility, suggesting differential access to TF networks (Figure S5B). The CD28 costimulation-induced decrease of *FOXP1 and TCF7* expression detected 24 h after activation resulted from increased DNA accessibility of promoter repressive regulatory elements (Figures 5C and S5C). CD27 costimulation increased *STAT1*, *TCF7*, and *CCR7* expression and was associated with increased DNA accessibility of promoter enhancing gene regions (Figures 5C, 5D, and S5D). CD28 but not CD27 costimulation broadly increased accessibility at *IFNG* and *IL2* promoter enhancing gene regions, two core transcriptional features of effector T cell differentiation[44] (Figures 5E and S5E). In line with a progressive acquisition of effector functions, αCD3+αCD28-stimulated Tn cells revealed distinct T-box transcription factor 21 (TBX21), NF of activated Tn cells 2 (NFATC2), FOS and JUN motif footprints, which were completely absent or attenuated in αCD3+CD70^{DT}-activated cells (Figures 5F and S5F).

By integrating transcriptomic and motif accessibility data, we were able to identify putative TF regulators and target genes in resting Tn cells and 24-h-activated Tn cells (Figure S5G). We observed that αCD3+αCD28 activation resulted in overall broad TF motif accessibility that was only correlated with transcript levels in a subset of candidates (Figure S5H). In order to infer highly utilized TFs, we correlated transcript levels with motif accessibility. A particularly high positive correlation score was obtained in naive and 24 h αCD3+CD70^{DT}-activated Tn cells for TF regulatory element activating TF 2 (ATF2),[45] the T cell quiescence regulator FOXP1,[35,36] and the FOX Protein TFs J3 (FOXJ3) and O1 (FOXO1), both occupying an enhancer located upstream of the TCF1 locus and implicated in memory formation.[46,47] However, 24 h αCD3+αCD28-activated Tn cells showed strong positive correlation for TBX21, MYC-associated zinc-finger protein (MAZ) and NFATC2, indicative of enhanced effector programming (Figure 5G). Lastly, we looked at inferred TF target genes in resting Tn cells and 24 h-activated Tn cells to confirm gene regulatory network specificity. Analysis showed that the ATF2 network was induced in 24 h αCD3+CD70^{DT}-activated cells when compared with naive cells. Consistent with the low transcript-to-motif correlation (Figure 5G), interference-based ATF2 utilization was reduced in response to 24 h αCD3+αCD28 activation. Further, we observed particularly high utilization of quiescence- and stemness-associated TFs including FOXJ3, FOXP1, FOXO1, TCF7, and LEF1 in Tn cells. As expected, 24 h αCD3+αCD28-activated T cells showed significantly reduced utilization of these circuits.

(H) Seahorse-based mitochondrial stress test (left) assessing changes in oxygen consumption rate (OCR) and (right) measuring spare respiratory capacity ofTn cells 10 days after stimulation (1 donor à 10 replicate wells). Oligomycin (oligo), phenylhydrazone (FCCP), and rotenone and antimycine A (Rot + AA) were added as indicated. All data are shown as mean ± SEM and were analyzed by two-way ANOVA (A, B, and F), paired (C–E) and unpaired (G and H) two-tailed Student's t test *p < 0.05, **p < 0.01, ***p < 0.005, ****p < 0.001. Illustration (A) created using BioRender. See also Figure S4.

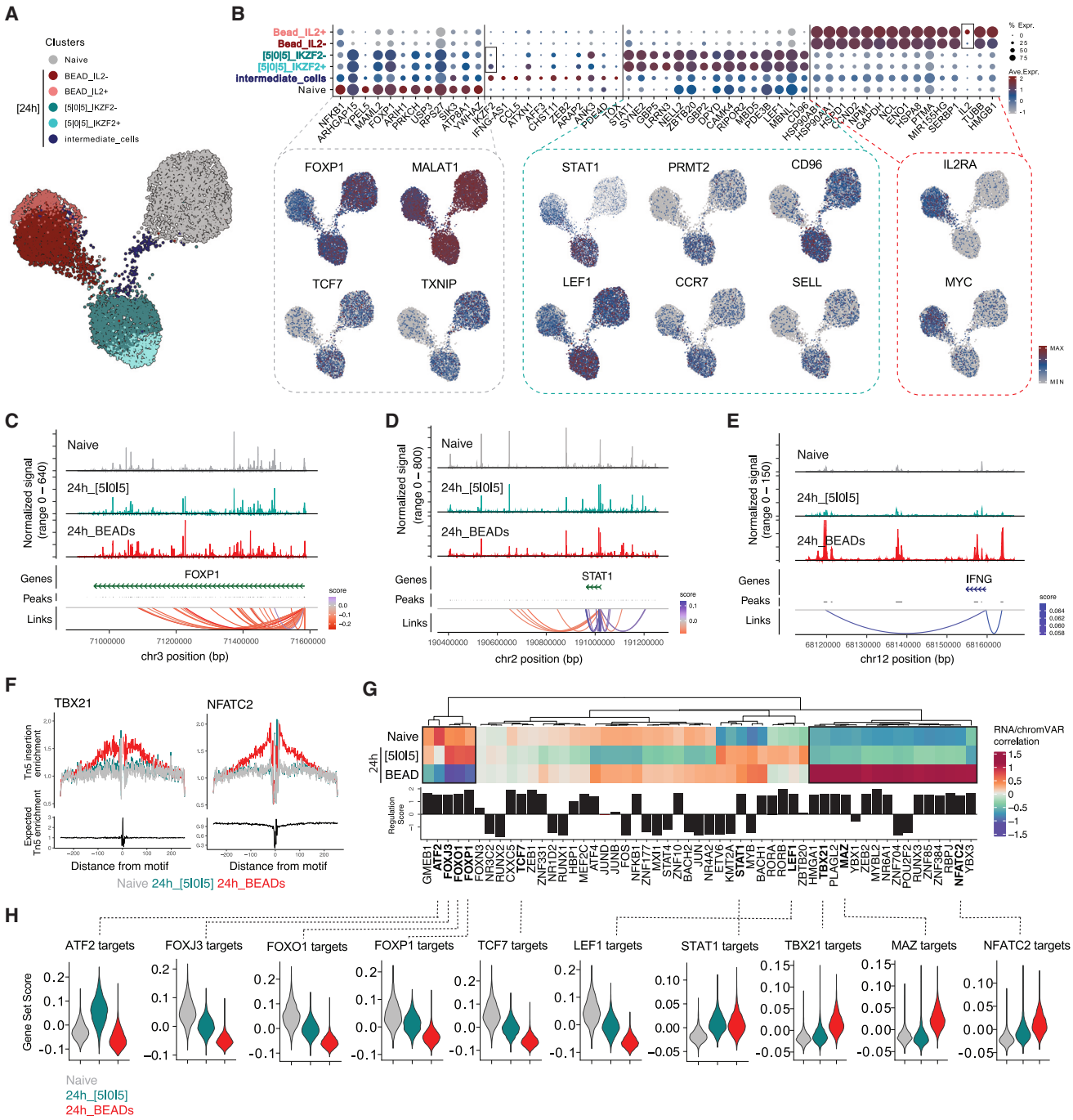

Figure 5. CD27 costimulation induces distinct gene regulatory circuits early after T cell activation

Single-cell multiome-seq of Tn cells that are non-activated (n.a.) and activated for 24 h with αCD3+αCD28 beads [at 3:1 bead:cell ratio] or plate-coated αCD3+αCD28+CD70^{DT} ([5|0|5]; μg/mL) (n = 1 donor).

(A and B) (A) Subclustered UMAP and (B) top differentially expressed genes in respective subclusters of single-cell RNA-seq data.

(C–F) ATAC-seq of the 3 main clusters showing (C–E) coverage plots of FOXP1, STAT1, and IFNG gene loci and linked (red, repressive; blue, activating) promoter regulatory gene peaks.

(F) ATAC-footprints of TBX21 and NFATC2 transcription factor motifs.

(G and H) Combined RNA-seq and ATAC-seq showing (G) heatmap-based correlation of RNA expression to DNA accessibility of indicated top-regulated transcription factors and (H) inferred target gene regulation of selected transcription factors. See also Figures S5 and S6.

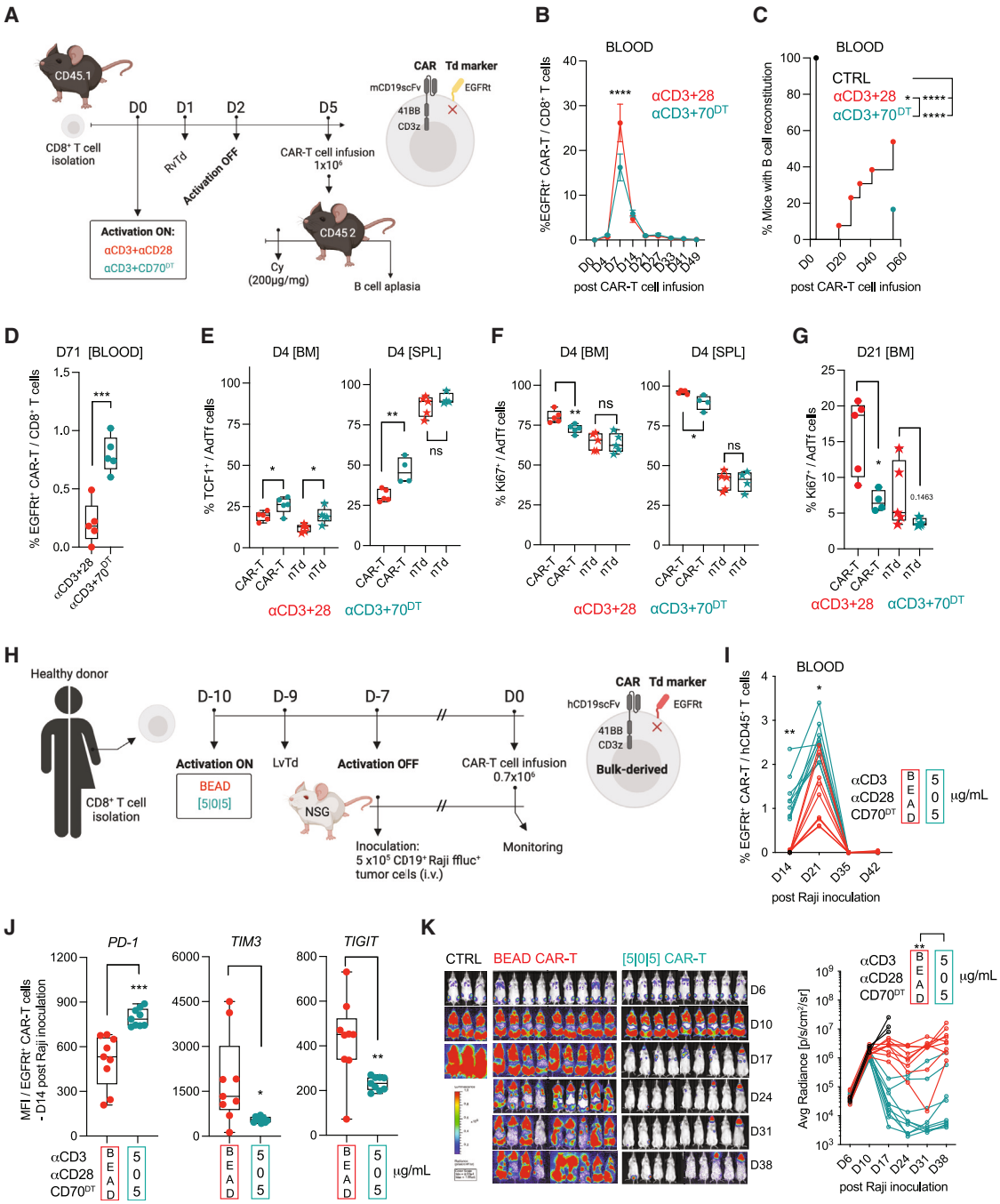

Figure 6. CD27 costimulation of CAR-T cells during manufacturing improves *in vivo* function

(A) Murine B cell aplasia model. Murine CD45.1$^+$CD8$^+$ T cells were isolated from spleen, activated with plate-coated αCD3 (1 μg/mL) and αCD28 or CD70^{DT} (each at 1 μg/mL), transduced with a retrovirus encoding mCD19_4-1BB_CD3ζ CAR and EGFRt (transduction marker), and transferred at a cell dose of 1 × 10^6 into lymphodepleted (Cytoxan) CD45.2$^+$ C57BL/6 mice.

(B) Quantification of percent (%) EGFRt$^+$CD8$^+$ CAR-T cells in peripheral blood of mice (n = 12–13, 2 pooled experiments).

(C) Monitoring of CD19$^+$ B cells in the peripheral blood of CAR-T cell infused or control mice (B cell reconstitution cut-off ≥ 1%).

(D) Quantification of EGFRt$^+$CD8$^+$ CAR-T cells in peripheral blood of mice 71 days post infusion (n = 5 mice).

(E–G) (E) TCF1 and (F and G) Ki67 expression in EGFRt$^+$CD45.1$^+$ or non-transduced (nTd) EGFRt$^-$CD45.1$^+$ T cells in BM and spleen harvested at day 4 (E and F) and BM harvested at day 21 (G) after adoptive transfer (AdTf) (n = 4–5 mice per time point and group).

(H) Raji-lymphoma xenograft model. Human bulk CD8$^+$ T cells were isolated from peripheral blood of healthy donors, activated with plate-coated αCD3+-αCD28+CD70^{DT} ([5|0|5]; μg/mL) or αCD3+αCD28 beads (at a 3:1 bead:cell ratio) before transduction with a lentivirus encoding a hCD19_4-1BB_CD3ζ CAR and EGFRt. T cells were transferred at a dose of 0.7 × 10^5 to tumor-bearing mice.

(I) Frequency of EGFRt$^+$CD8$^+$ CAR-T cells per total human CD45$^+$ T cells in peripheral blood of mice.

(legend continued on next page)

However, CD27 costimulation, but not CD28, preserved a stemness-like DNA architecture, limiting the transition toward effector differentiation. Consistent with acquisition of an activated T cell state, both CD27- and CD28-costimulated cells showed induction of STAT1 circuitry. Reflective of an effector differentiation state, CD28 costimulation strongly engaged TBX21, MAZ, and NFATC2 and enhanced target gene expression (Figure 5H). In summary, these data suggest that the epigenetic alterations evoked in response to CD27 costimulation enhances regulatory TF circuits that preserve a stem-like T cell state and hinder effector differentiation.

Given the observed modulatory role of CD27 costimulation when provided in combination with CD28 costimulation (Figure 3), we additionally analyzed the transcriptional states of Tn cells activated for 24 h with a combination of αCD3+αCD28 and two different doses of $CD70^{DT}$. Seurat clustering identified a total of 6 subclusters (Figure S6A). Subcluster 1 that was represented by resting Tn cells was connected via subcluster 2 with the remaining subclusters 3–6. While subcluster 6 was dominated by αCD3+αCD28 bead-activated cells, subcluster 3 was dominated by αCD3+$CD70^{DT}$-activated cells. T cells activated with αCD3+αCD28 and high $CD70^{DT}$ dose were mainly found in subclusters 4 and 5 which aligned in between subclusters 3 and 6. Tn cells activated with αCD3+αCD28 and low $CD70^{DT}$ dose were increasingly populated in the αCD3+αCD28 bead dominated cluster 6 (Figure S6B). Pseudotime-analysis revealed that resting Tn cell-associated signature genes such as *FOXO1*, *FOXP1*, *TCF7*, *LEF1*, *IL7R*, and *ZBTB20* showed a stepwise decrease of expression with transition from cluster 3 to 6. CD27 costimulation-associated signature genes (i.e., *CCR7*) were highest maintained in clusters 3 and 4, which was dominated by cells activated with αCD3+$CD70^{DT}$ or with high-dose $CD70^{DT}$ combined with αCD28. *GAPDH*, IL2RA and *ENO1* genes associated with effector differentiation were increasingly induced from clusters 3 to 6 (Figure S6C). We then asked whether these early transcriptional changes observed in response to CD27 costimulation would be reflected in a spectrum of effector versus memory cell surface phenotypes after 9 days in culture. Increasing the dose of CD27 costimulation with αCD3+αCD28 stimulation promoted the maintenance of $TCF1^{+}CD27^{+}$ cells with a $CD45RA^{hi}CD45RO^{low}CD25^{low}CD95^{hi}$ Tcm and Tscm phenotype (Figure S6D), but the highest recovery of T cells with memory characteristics resulted from activation with αCD3+$CD70^{DT}$ alone.

CD27 costimulation improves therapeutic efficacy of CAR-T cells

The differentiation state and metabolic fitness of T cells has been shown to affect their persistence and antitumor activity after adoptive transfer.[14,15] We first used a murine model to examine whether CD27 signaling affected the ability of T cells to sustain function under conditions of chronic antigen stimulation. As described for human Tn cells (see Figure 1), αCD3 and $CD70^{DT}$ stimulation of murine Tn cells induced rapid CD27 surface receptor down-modulation (Figure S7A). We generated murine CD19-targeting 41BB_CD3ζ CAR-T cells using αCD3+$CD70^{DT}$ or αCD3+αCD28 stimulation, adoptively transferred these into immunocompetent mice that were monitored for B cell aplasia, CAR-T cell persistence and phenotype (Figure 6A). Despite reaching only 50% of the peak frequency of αCD3+αCD28-stimulated CAR-T cells after adoptive transfer, αCD3+$CD70^{DT}$-stimulated CAR-T cells maintained B cell aplasia in more than 80% of mice, and persisted at high levels in blood compared with mice treated with αCD3+αCD28-stimulated CAR-T cells, which maintained B cell aplasia in only 40% of mice and persisted at lower levels at late time points (Figures 6B–6D). As early as 4 days after adoptive transfer, αCD3+$CD70^{DT}$-stimulated CAR-T cells present in BM and spleen expressed higher levels of TCF1 and had a lower fraction of $Ki67^{+}$ cells compared with those stimulated with αCD3+αCD28 (Figures 6E and 6F), and this difference in the $Ki67^{+}$ fraction was maintained in the BM through day 21 (Figure 6G). Fewer αCD3+$CD70^{DT}$-stimulated CAR-T cells in BM and spleen co-expressed inhibitory and activation markers ($PD1^{+}CD39^{+}$, $PD1^{+}TIM3^{+}$, $PD1^{+}TIGIT^{+}$) compared with -αCD3+αCD28-stimulated T cells (Figure S7B). These data show that in this model of chronic antigen stimulation, αCD3+$CD70^{DT}$-stimulated CD19 CAR-T cells more durably eliminate endogenous $CD19^{+}$ B cells than αCD3+αCD28-stimulated CAR-T cells.

We next evaluated the therapeutic activity of human CD19-targeting CAR-T cells in a human tumor xenograft model. 4-1BB_CD3ζ CD19 CAR-T cells were derived from unselected bulk $CD8^{+}$ T cells after activation with plate-coated αCD3+$CD70^{DT}$ or with αCD3+αCD28 beads, the latter approach commonly used for stimulation in clinical CAR-T cell therapy. Cohorts of NSG mice were inoculated with $CD19^{+}$ $ffluc^{+}$ Raji-lymphoma cell line and treated 7 days later with either αCD3+$CD70^{DT}$ CAR-T cells or αCD3+αCD28 CAR-T cells at a sub-curative dose (Figure 6H). In contrast to the murine chronic antigen stimulation model, αCD3+$CD70^{DT}$-stimulated CAR-T cells expanded to higher numbers than αCD3+αCD28 CAR-T cells in this tumor model (Figure 6I). Before reaching the peak of expansion, αCD3+$CD70^{DT}$-stimulated CAR-T cells expressed increased levels of PD-1 but lower levels of inhibitory markers TIM3 and TIGIT (Figure 6J), which resulted in more effective elimination of Raji tumor cells (Figure 6K).

The superior efficacy targeting hematopoietic cells in murine and human models suggested that CD27 signaling might generate CAR-T cells that would be more effective against solid tumors. To assess the ability of αCD3+$CD70^{DT}$ to sustain killing of solid tumor cells we stimulated ROR1-specific 4-1BB_CD3ζ CAR-T cells with αCD3+$CD70^{DT}$ or αCD3+αCD28 and performed serial restimulations with $ROR1^{+}$ H1703 tumor cells without adjustment of E:T ratios (Figures S8A and S8B). αCD3+$CD70^{DT}$ CAR-T cells exhibited improved serial killing capacity compared with αCD3+CD28 CAR-T cells, despite showing reduced fold expansion, implicating an improved per-cell cytolytic capacity (Figures S8C and S8D). Analysis

(J) Mean Fluorescent Intensity (MFI) of PD-1, TIM3 and TIGIT on peripheral blood $EGFRt^{+}CD8^{+}$ CAR-T cells 7 days post infusion.
(K) Bioluminescence imaging of $ffluc^{+}$ Raji cells in control (untreated) or CAR-T cell-treated mice.
(I–K) n = 9 mice per group. All data are shown as mean ± SEM and were analyzed by log-rank (Mantle-Cox) test (C), Turkey's multiple comparison test (B and I), unpaired two-tailed Student's t test (D–G and J), and two-way ANOVA (K). *p < 0.05, **p < 0.01, ***p < 0.005, ****p < 0.001. Illustrations (A and H) created using BioRender. See also Figures S7 and S8.

of CAR-T cells after the 4th re-stimulation revealed that αCD3+CD70^{DT} CAR-T cells maintained higher cytokine secretion capacity, expressed elevated levels of the cytolytic and activation markers GZMB and 4-1BB, and acquired a less exhausted phenotype (Figures S8E and S8F). We then evaluated ROR1-directed αCD3+CD70^{DT} and αCD3+CD28 CAR-T cells in a ROR1^{+} breast-cancer xenograft model. Cohorts of NSG mice were inoculated with ROR1^{+} ffluc^{+} MDA-MB-231 cell line and treated 7 days later with Tn-derived CAR-T cells (Figure S8G). Mice receiving αCD3+CD70^{DT} CAR-T cells showed prolonged tumor control whereas progressive tumor outgrowth was observed in αCD3+CD28 CAR-T cell-treated mice around 18 days post infusion (Figure S8H). Moreover, CAR-T cell expansion was higher in mice treated with αCD3+CD70^{DT} CAR-T cells compared with αCD3+CD28 CAR-T cells (Figure S8I). Taken together, these data show that αCD3+CD70^{DT}-stimulated CAR-T cells possess a superior ability to sustain killing and function compared with αCD3+αCD28-stimulated CAR-T cells, as evaluated in the context of chronic and acute antigen exposure models.

DISCUSSION

CD27 is expressed on T cells and engaged during an immune response by APCs that transiently express CD70.[9] Signaling is further regulated by extracellular CD27 receptor cleavage that occurs beginning 24 h after ligand binding.[17,18] The importance of regulating cellular responses mediated by CD27 is illustrated by the observation that transgenic mice in which CD70 is constitutively expressed in B cells exhibit T cell effector differentiation, exhaustion, and lethal immunodeficiency.[48] Our studies using a synthetic trimeric CD70 ligand to transiently bind CD27 during Tn cell activation *in vitro* demonstrate that CD27 is rapidly internalized by CME after ligand engagement, identifying an immediate ligand-dependent mechanism to regulate the duration of CD27 signaling. Rapid internalization of CD27 was observed in co-cultures with CD70 expressing artificial APCs and with mature BM-derived DCs presenting antigen on major histocompatibility complex (MHC) molecules, demonstrating the physiological relevance of rapid ligand-induced CD27 endocytosis. CD27 expressed in more differentiated memory T cell subsets was also internalized, although the magnitude of endocytosis was reduced, suggesting that CD27 costimulation may be modulated differently in these subsets.

We found that ligating CD27 with higher doses of CD70^{DT} led to more TRAF2 being bound to CD27, which may provide a scaffold to build the receptor signalosome, similar to that described for TNFR 4-1BB.[49] Our studies show that TRAF2 is associated with SHP-1 and that this complex modulates Tn cell activation when CD28 is engaged, by inhibiting phosphorylation of Lck and reducing phosphorylation of ERK1/2 and AKT. This finding has parallels to the observation using a cell-free membrane reconstitution system that activation of PD-1 and SHP-2 inhibits T cells by de-phosphorylation of CD28 and Lck.[50] Our data show that the CD27-TRAF2-SHP-1 axis modulates the strength of activation induced by TCR and CD28 signals only when CD70-mediated CD27 engagement is sufficient to induce rapid CD27 endocytosis, preserving the ability of primed Tn cells to differentiate along a memory rather than effector fate. Notably, when activated Tn cells received a dose of CD70^{DT} that was insufficient to induce rapid endocytosis, ERK1/2 phosphorylation and T cell proliferation was enhanced. These data suggest that alternative signaling mechanisms are activated depending on the level of CD27 engagement.

CD27 costimulation transiently delayed cell cycle progression and altered metabolic and cell surface phenotype of T cells toward a Tscm and Tcm phenotype. This finding is in line with the observations that the formation of memory CD8^{+} T cells is marked by their slow replicative history.[51,52] As early as 24 h after Tn cell activation, CD27 signaling promoted a distinct transcriptional and epigenetic profile characterized by reduced expression of genes associated with effector differentiation, contrasting that observed with CD28 costimulation. T cells receiving TCR, CD28 and CD27 signals adopted a transcriptional profile that was intermediate to that observed with αCD3+CD70^{DT} or αCD3+αCD28 stimulation, implying that the strength of these signals cooperate to diversify T cell fates. 24 h CD27-costimulated Tn cells showed high utilization of TFs FOXO1, FOXP1, TCF1, and LEF1. These TF proteins are among the top 5 most rapidly turned over in quiescent Tn cells.[53] This suggests that induction of high TCF7 transcript levels in response to αCD3+CD70^{DT} activation may allow maintenance of high TCF1 protein levels despite high turnover of this TF. In contrast, αCD3+αCD28-activated Tn cells may fail to maintain TCF1 protein levels due to lower TCF7 transcript expression, despite having broadly accessible DNA-binding motifs. FOXO1 is known to constrain CD8^{+} Tn cell activation by attenuating AP-1 effector programs[54] and is required for formation of Tcm in part by regulating the TCF7 gene locus.[46] Further, our findings raise the question whether the observed CD27 signaling-induced FOXP1 regulatory network is conserved across T cell lineages, given that CD4^{+} Treg cell differentiation and identity are associated with both CD27 signaling[55] and FOXP1 transcriptional regulation.[56]

Our data illustrating that CD27 costimulation of αCD3-activated Tn cells promotes the acquisition of memory properties led us to evaluate a new strategy for manufacturing of therapeutic T cell products. Disease relapse after CAR-T cell therapy targeting CD19 or BCMA can occur due to lack of CAR-T cell persistence, function or a combination of both. In some cases this may reflect a suboptimal quality of the expanded CAR-T infusion product.[15] By engaging the CD27 costimulatory receptor, we were able to enrich the infusion product with T cells characterized by a less effector-differentiated state, which in turn persisted better under chronic antigen stimulation and mediated superior antitumor effects *in vivo* compared with αCD3+αCD28-activated CAR-T cells. Thus, CD27 costimulation could provide a qualitative advantage during CAR-T cell manufacturing and improve long-term CAR-T cell therapeutic efficacy.

Limitations of the study

Our data show that CD28 is required for the modulatory effects of CD70^{DT} on Lck and ERK1/2 phosphorylation in activated Tn cells but does not address whether the affected Lck is associated with CD28 or with other binding partners. It is also unknown whether varlilumab, an agonistic CD27 mAb that has been in the clinic, would have similar effects to the natural CD70 ligand. Endocytosis of CD27, which is greater with more engagement by

$CD70^{DT}$, is required for the effects on LCK and ERK1/2 phosphorylation; however, we did not evaluate alternative signaling mechanisms from non-endocytosed CD27 when a lower amount of CD27 is engaged by $CD70^{DT}$. Although we demonstrate that the level CD70 on murine DC and CD70-transgene expressing K32 cells is sufficient for CD27 internalization, a limitation of our study is that the signaling work was largely performed using $CD70^{DT}$ and agonistic antibodies. Additional studies examining the consequences of CD70 interactions with CD27 *in vivo* are necessary. We compared αCD3+αCD28 beads with αCD3+$CD70^{DT}$ for generating CAR-T cells because we observed the greatest preservation of memory properties with αCD3+$CD70^{DT}$ compared with activation conditions that included αCD28. Although efficacy of CAR-T cells has been associated with memory properties, the active ingredient(s) in heterogeneous T cell products that confer treatment efficacy after adoptive cell therapy are incompletely defined. Other stimulation conditions for generating therapeutic T cells that include different doses of $CD70^{DT}$ and αCD28 might be beneficial and should be evaluated in future studies. Finally, the multi-ome analysis of Tn cells receiving αCD3+αCD28, αCD3+αCD28+$CD70^{DT}$, and αCD3+$CD70^{DT}$ stimulation was performed at a single time point. This analysis captures early differences resulting from these different activation signals but does not describe differences in transcriptional or epigenetic trajectories that may emerge later.

STAR★METHODS

Detailed methods are provided in the online version of this paper and include the following:

- KEY RESOURCES TABLE
- RESOURCE AVAILABILITY
  - Lead contact
  - Materials availability
  - Data and code availability
- EXPERIMENTAL MODEL AND STUDY PARTICIPANT DETAILS
  - Mice
  - Human subjects
  - Cell lines
- METHOD DETAILS
  - Recombinant protein design, production and modelling
  - CAR construction and virus production
  - T cell isolation, activation and viral transduction
  - Xenograft and B-cell aplasia models
  - Serial restimulation assay
  - Flow cytometry
  - Generation of BM-derived DCs
  - Immune co-culture with APCs
  - Internalization and cleavage assay
  - Protein degradation assay
  - Metabolic assays
  - Proliferation and cell cycle analysis
  - Glucose tracing
  - LC-MS metabolite quantification
  - Gene deletion in resting human Tn cells
  - Single-cell RNA and ATAC sequencing
  - Single-cell RNA and ATAC computational analysis
  - Western blot assay
  - Immunoprecipitation assay
  - Quantitative PCR
- QUANTIFICATION AND STATISTICAL ANALYSIS
  - Statistical analysis

SUPPLEMENTAL INFORMATION

Supplemental information can be found online at https://doi.org/10.1016/j.immuni.2024.01.011.

ACKNOWLEDGMENTS

This work was supported by grants from the NIH P01 CA18029 and R01 CA114536 (to S.R.R.), NCI P30 CA015704 Cancer Center Support Grant, LLS 7023-20 Leukemia and Lymphoma Society and Lyell Immunopharma. We wish to thank Margot Pont, Sophia Schreiber, and Naina Singhi for supportive discussions. Furthermore, we wish to thank Don Parilla, Ekram A. Gad, and Latrice King from the Comparative Medicine Shared Resource team for the support with mouse experiments. This research was supported by the Cellular Imaging Shared Resource RRID: SCR_022609 of the Fred Hutch, University of Washington Cancer Consortium (P30CA015704). For technical support, we wish to thank Lena Schroeder, Hoku West-Foyle, and Jin Meng from the Cellular Imaging Shared Resource team as well as Michele Black, Andrew Berger, Rebecca Reeves, and Ben Janoschek from the Flow Cytometry Shared Resource team. Illustrated figures were created with BioRender.

AUTHOR CONTRIBUTIONS

Conceptualization, C.A.J.-R. and S.R.R.; methodology, C.A.J.-R., S.R.R., T.B.S., S.S., S.N.F., and L.B.S.; validation, C.A.J.-R., S.R.R., Y.L., E.F., S.N.F., and L.B.S.; investigation, C.A.J.-R., T.B.S., Y.L., E.F., S.B.K., O.J.N., I.A.E., S.S.B., J.M.C.P., A.R.S., S.M.S., V.M., G.B., and M.G.K.; resources, C.E.C., R.R., J.P.P., J.M.O., F.M., J.F.S., S.H., V.V., and R.G.; data curation, O.G.W. and P.V.M.; writing – original draft, C.A.J.-R. and S.R.R.; visualization, C.A.J.-R.; supervision, S.R.R.; project administration, C.A.J.-R.; funding acquisition, C.A.J.-R. and S.R.R.

DECLARATION OF INTERESTS

C.A.J.-R., C.E.C., and S.R.R. are inventors on a patent (“engineered trimeric CD70 proteins and uses thereof”; WO2021072127A3) filed by Fred Hutchinson Cancer Center and licensed by Lyell Immunopharma. S.R.R. was a founder, has served as an advisor, and has patents licensed to Juno Therapeutics; S.R.R is a founder of and holds equity in Lyell Immunopharma and has served on the advisory boards for Adaptive Biotechnologies and Nohla.

Received: February 27, 2023
Revised: September 26, 2023
Accepted: January 11, 2024
Published: February 13, 2024

REFERENCES

1. Wiesmann, A., Phillips, R.L., Mojica, M., Pierce, L.J., Searles, A.E., Spangrude, G.J., and Lemischka, I. (2000). Expression of CD27 on murine hematopoietic stem and progenitor cells. Immunity *12*, 193–199.
2. Hintzen, R.Q., de Jong, R., Lens, S.M., Brouwer, M., Baars, P., and van Lier, R.A. (1993). Regulation of CD27 expression on subsets of mature T-lymphocytes. J. Immunol. *151*, 2426–2435.
3. van Lier, R.A., Borst, J., Vroom, T.M., Klein, H., Van Mourik, P., Zeijlemaker, W.P., and Melief, C.J. (1987). Tissue distribution and biochemical and functional properties of Tp55 (CD27), a novel T cell differentiation antigen. J. Immunol. *139*, 1589–1596.

4. Hamann, D., Baars, P.A., Rep, M.H., Hooibrink, B., Kerkhof-Garde, S.R., Klein, M.R., and van Lier, R.A. (1997). Phenotypic and functional separation of memory and effector human CD8+ T cells. J. Exp. Med. *186*, 1407–1418.

5. Gattinoni, L., Speiser, D.E., Lichterfeld, M., and Bonini, C. (2017). T memory stem cells in health and disease. Nat. Med. *23*, 18–27.

6. Hendriks, J., Gravestein, L.A., Tesselaar, K., van Lier, R.A., Schumacher, T.N., and Borst, J. (2000). CD27 is required for generation and long-term maintenance of T cell immunity. Nat. Immunol. *1*, 433–440.

7. Liu, W., Maben, Z., Wang, C., Lindquist, K.C., Li, M., Rayannavar, V., Lopez Armenta, I., Nager, A., Pascua, E., Dominik, P.K., et al. (2021). Structural delineation and phase-dependent activation of the costimulatory CD27:CD70 complex. J. Biol. Chem. *297*, 101102.

8. Hintzen, R.Q., Lens, S.M., Lammers, K., Kuiper, H., Beckmann, M.P., and van Lier, R.A. (1995). Engagement of CD27 with its ligand CD70 provides a second signal for T cell activation. J. Immunol. *154*, 2612–2623.

9. Keller, A.M., Groothuis, T.A., Veraar, E.A., Marsman, M., Maillette de Buy Wenniger, L., Janssen, H., Neefjes, J., and Borst, J. (2007). Costimulatory ligand CD70 is delivered to the immunological synapse by shared intracellular trafficking with MHC class II molecules. Proc. Natl. Acad. Sci. USA *104*, 5989–5994.

10. Akiba, H., Nakano, H., Nishinaka, S., Shindo, M., Kobata, T., Atsuta, M., Morimoto, C., Ware, C.F., Malinin, N.L., Wallach, D., et al. (1998). CD27, a member of the tumor necrosis factor receptor superfamily, activates NF-kappaB and stress-activated protein kinase/c-Jun N-terminal kinase via TRAF2, TRAF5, and NF-kappaB-inducing kinase. J. Biol. Chem. *273*, 13353–13358.

11. Jaeger-Ruckstuhl, C.A., Hinterbrandner, M., Höpner, S., Correnti, C.E., Lüthi, U., Friedli, O., Freigang, S., Al Sayed, M.F., Bührer, E.D., Amrein, M.A., et al. (2020). TNIK signaling imprints $CD8^+$ T cell memory formation early after priming. Nat. Commun. *11*, 1632.

12. Gattinoni, L., Klebanoff, C.A., and Restifo, N.P. (2012). Paths to stemness: building the ultimate antitumour T cell. Nat. Rev. Cancer *12*, 671–684.

13. June, C.H., O'Connor, R.S., Kawalekar, O.U., Ghassemi, S., and Milone, M.C. (2018). CAR T cell immunotherapy for human cancer. Science *359*, 1361–1365.

14. Fraietta, J.A., Lacey, S.F., Orlando, E.J., Pruteanu-Malinici, I., Gohil, M., Lundh, S., Boesteanu, A.C., Wang, Y., O'Connor, R.S., Hwang, W.T., et al. (2018). Determinants of response and resistance to CD19 chimeric antigen receptor (CAR) T cell therapy of chronic lymphocytic leukemia. Nat. Med. *24*, 563–571.

15. Deng, Q., Han, G., Puebla-Osorio, N., Ma, M.C.J., Strati, P., Chasen, B., Dai, E., Dang, M., Jain, N., Yang, H., et al. (2020). Characteristics of anti-CD19 CAR T cell infusion products associated with efficacy and toxicity in patients with large B cell lymphomas. Nat. Med. *26*, 1878–1887.

16. Correnti, C.E., Hallinan, J.P., Doyle, L.A., Ruff, R.O., Jaeger-Ruckstuhl, C.A., Xu, Y., Shen, B.W., Qu, A., Polkinghorn, C., Friend, D.J., et al. (2020). Engineering and functionalization of large circular tandem repeat protein nanoparticles. Nat. Struct. Mol. Biol. *27*, 342–350.

17. Hintzen, R.Q., de Jong, R., Hack, C.E., Chamuleau, M., de Vries, E.F., ten Berge, I.J., Borst, J., and van Lier, R.A. (1991). A soluble form of the human T cell differentiation antigen CD27 is released after triggering of the TCR/CD3 complex. J. Immunol. *147*, 29–35.

18. Hintzen, R.Q., Lens, S.M., Beckmann, M.P., Goodwin, R.G., Lynch, D., and van Lier, R.A. (1994). Characterization of the human CD27 ligand, a novel member of the TNF gene family. J. Immunol. *152*, 1762–1773.

19. Maus, M.V., Thomas, A.K., Leonard, D.G., Allman, D., Addya, K., Schlienger, K., Riley, J.L., and June, C.H. (2002). Ex vivo expansion of polyclonal and antigen-specific cytotoxic T lymphocytes by artificial APCs expressing ligands for the T-cell receptor, CD28 and 4–1BB. Nat. Biotechnol. *20*, 143–148.

20. Schneider-Brachert, W., Tchikov, V., Neumeyer, J., Jakob, M., Winoto-Morbach, S., Held-Feindt, J., Heinrich, M., Merkel, O., Ehrenschwender, M., Adam, D., et al. (2004). Compartmentalization of TNF receptor 1 signaling: internalized TNF receptosomes as death signaling vesicles. Immunity *21*, 415–428.

21. Schütze, S., Tchikov, V., and Schneider-Brachert, W. (2008). Regulation of TNFR1 and CD95 signalling by receptor compartmentalization. Nat. Rev. Mol. Cell Biol. *9*, 655–662.

22. Taylor, M.J., Perrais, D., and Merrifield, C.J. (2011). A high precision survey of the molecular dynamics of mammalian clathrin-mediated endocytosis. PLoS Biol. *9*, e1000604.

23. Yamamoto, H., Kishimoto, T., and Minamoto, S. (1998). NF-kappaB activation in CD27 signaling: involvement of TNF receptor-associated factors in its signaling and identification of functional region of CD27. J. Immunol. *161*, 4753–4759.

24. Choi, S., Warzecha, C., Zvezdova, E., Lee, J., Argenty, J., Lesourne, R., Aravind, L., and Love, P.E. (2017). THEMIS enhances TCR signaling and enables positive selection by selective inhibition of the phosphatase SHP-1. Nat. Immunol. *18*, 433–441.

25. Chiang, G.G., and Sefton, B.M. (2001). Specific dephosphorylation of the Lck tyrosine protein kinase at Tyr-394 by the SHP-1 protein-tyrosine phosphatase. J. Biol. Chem. *276*, 23173–23178.

26. Holdorf, A.D., Lee, K.H., Burack, W.R., Allen, P.M., and Shaw, A.S. (2002). Regulation of Lck activity by CD4 and CD28 in the immunological synapse. Nat. Immunol. *3*, 259–264.

27. Lovatt, M., Filby, A., Parravicini, V., Werlen, G., Palmer, E., and Zamoyska, R. (2006). Lck regulates the threshold of activation in primary T cells, while both Lck and Fyn contribute to the magnitude of the extracellular signal-related kinase response. Mol. Cell. Biol. *26*, 8655–8665.

28. Cuevas, B., Lu, Y., Watt, S., Kumar, R., Zhang, J., Siminovitch, K.A., and Mills, G.B. (1999). SHP-1 regulates Lck-induced phosphatidylinositol 3-kinase phosphorylation and activity. J. Biol. Chem. *274*, 27583–27589.

29. Colombetti, S., Basso, V., Mueller, D.L., and Mondino, A. (2006). Prolonged TCR/CD28 engagement drives IL-2-independent T cell clonal expansion through signaling mediated by the mammalian target of rapamycin. J. Immunol. *176*, 2730–2738.

30. Pais Ferreira, D., Silva, J.G., Wyss, T., Fuertes Marraco, S.A., Scarpellino, L., Charmoy, M., Maas, R., Siddiqui, I., Tang, L., Joyce, J.A., et al. (2020). Central memory $CD8^+$ T cells derive from stem-like Tcf7(hi) effector cells in the absence of cytotoxic differentiation. Immunity *53*, 985–1000.e11.

31. Chi, H. (2012). Regulation and function of mTOR signalling in T cell fate decisions. Nat. Rev. Immunol. *12*, 325–338.

32. Sukumar, M., Liu, J., Ji, Y., Subramanian, M., Crompton, J.G., Yu, Z., Roychoudhuri, R., Palmer, D.C., Muranski, P., Karoly, E.D., et al. (2013). Inhibiting glycolytic metabolism enhances CD8+ T cell memory and antitumor function. J. Clin. Invest. *123*, 4479–4488.

33. Fischer, M., Bantug, G.R., Dimeloe, S., Gubser, P.M., Burgener, A.V., Grählert, J., Balmer, M.L., Develioglu, L., Steiner, R., Unterstab, G., et al. (2018). Early effector maturation of naive human $CD8^+$ T cells requires mitochondrial biogenesis. Eur. J. Immunol. *48*, 1632–1643.

34. Zhang, H., Jadhav, R.R., Cao, W., Goronzy, I.N., Zhao, T.V., Jin, J., Ohtsuki, S., Hu, Z., Morales, J., Greenleaf, W.J., et al. (2023). Aging-associated HELIOS deficiency in naive CD4(+) T cells alters chromatin remodeling and promotes effector cell responses. Nat. Immunol. *24*, 96–109.

35. Feng, X., Wang, H., Takata, H., Day, T.J., Willen, J., and Hu, H. (2011). Transcription factor Foxp1 exerts essential cell-intrinsic regulation of the quiescence of naive T cells. Nat. Immunol. *12*, 544–550.

36. Wei, H., Geng, J., Shi, B., Liu, Z., Wang, Y.H., Stevens, A.C., Sprout, S.L., Yao, M., Wang, H., and Hu, H. (2016). Cutting Edge: Foxp1 Controls Naive CD8+ T Cell Quiescence by Simultaneously Repressing Key Pathways in Cellular Metabolism and Cell Cycle Progression. J. Immunol. *196*, 3537–3541.

37. Zhao, X., Shan, Q., and Xue, H.H. (2022). TCF1 in T cell immunity: a broadened frontier. Nat. Rev. Immunol. *22*, 147–157.

38. Wu, N., Zheng, B., Shaywitz, A., Dagon, Y., Tower, C., Bellinger, G., Shen, C.H., Wen, J., Asara, J., McGraw, T.E., et al. (2013). AMPK-dependent

degradation of TXNIP upon energy stress leads to enhanced glucose uptake via GLUT1. Mol. Cell *49*, 1167–1175.

39. Kanbar, J.N., Ma, S., Kim, E.S., Kurd, N.S., Tsai, M.S., Tysl, T., Widjaja, C.E., Limary, A.E., Yee, B., He, Z., et al. (2022). The long noncoding RNA Malat1 regulates CD8+ T cell differentiation by mediating epigenetic repression. J. Exp. Med. *219*.
40. Ramana, C.V., Chatterjee-Kishore, M., Nguyen, H., and Stark, G.R. (2000). Complex roles of Stat1 in regulating gene expression. Oncogene *19*, 2619–2627.
41. Ohmori, Y., Schreiber, R.D., and Hamilton, T.A. (1997). Synergy between interferon-gamma and tumor necrosis factor-alpha in transcriptional activation is mediated by cooperation between signal transducer and activator of transcription 1 and nuclear factor kappaB. J. Biol. Chem. *272*, 14899–14907.
42. Kye, Y.C., Lee, G.W., Lee, S.W., Ju, Y.J., Kim, H.O., Yun, C.H., and Cho, J.H. (2021). STAT1 maintains naive CD8$^+$ T cell quiescence by suppressing the type I IFN-STAT4-mTORC1 signaling axis. Sci. Adv. *7*, eabg8764.
43. Chiang, E.Y., de Almeida, P.E., de Almeida Nagata, D.E., Bowles, K.H., Du, X., Chitre, A.S., Banta, K.L., Kwon, Y., McKenzie, B., Mittman, S., et al. (2020). CD96 functions as a co-stimulatory receptor to enhance CD8$^+$ T cell activation and effector responses. Eur. J. Immunol. *50*, 891–902.
44. Kaech, S.M., and Cui, W. (2012). Transcriptional control of effector and memory CD8+ T cell differentiation. Nat. Rev. Immunol. *12*, 749–761.
45. Watson, G., Ronai, Z.A., and Lau, E. (2017). ATF2, a paradigm of the multifaceted regulation of transcription factors in biology and disease. Pharmacol. Res. *119*, 347–357.
46. Kim, M.V., Ouyang, W., Liao, W., Zhang, M.Q., and Li, M.O. (2013). The transcription factor Foxo1 controls central-memory CD8+ T cell responses to infection. Immunity *39*, 286–297.
47. He, B., Xing, S., Chen, C., Gao, P., Teng, L., Shan, Q., Gullicksrud, J.A., Martin, M.D., Yu, S., Harty, J.T., et al. (2016). CD8$^+$ T Cells Utilize Highly Dynamic Enhancer Repertoires and Regulatory Circuitry in Response to Infections. Immunity *45*, 1341–1354.
48. Tesselaar, K., Arens, R., van Schijndel, G.M., Baars, P.A., van der Valk, M.A., Borst, J., van Oers, M.H., and van Lier, R.A. (2003). Lethal T cell immunodeficiency induced by chronic costimulation via CD27-CD70 interactions. Nat. Immunol. *4*, 49–54.
49. Zapata, J.M., Perez-Chacon, G., Carr-Baena, P., Martinez-Forero, I., Azpilikueta, A., Otano, I., and Melero, I. (2018). CD137 (4-1BB) Signalosome: Complexity Is a Matter of TRAFs. Front. Immunol. *9*, 2618.
50. Hui, E., Cheung, J., Zhu, J., Su, X., Taylor, M.J., Wallweber, H.A., Sasmal, D.K., Huang, J., Kim, J.M., Mellman, I., et al. (2017). T cell costimulatory receptor CD28 is a primary target for PD-1-mediated inhibition. Science *355*, 1428–1433.
51. Kretschmer, L., Flossdorf, M., Mir, J., Cho, Y.L., Plambeck, M., Treise, I., Toska, A., Heinzel, S., Schiemann, M., Busch, D.H., et al. (2020). Differential expansion of T central memory precursor and effector subsets is regulated by division speed. Nat. Commun. *11*, 113.
52. Bresser, K., Kok, L., Swain, A.C., King, L.A., Jacobs, L., Weber, T.S., Perié, L., Duffy, K.R., de Boer, R.J., Scheeren, F.A., et al. (2022). Replicative history marks transcriptional and functional disparity in the CD8$^+$ T cell memory pool. Nat. Immunol. *23*, 791–801.
53. Wolf, T., Jin, W., Zoppi, G., Vogel, I.A., Akhmedov, M., Bleck, C.K.E., Beltraminelli, T., Rieckmann, J.C., Ramirez, N.J., Benevento, M., et al. (2020). Dynamics in protein translation sustaining T cell preparedness. Nat. Immunol. *21*, 927–937.
54. Delpoux, A., Marcel, N., Hess Michelini, R., Katayama, C.D., Allison, K.A., Glass, C.K., Quiñones-Parra, S.M., Murre, C., Loh, L., Kedzierska, K., et al. (2021). FOXO1 constrains activation and regulates senescence in CD8 T cells. Cell Rep. *34*, 108674.
55. Coquet, J.M., Ribot, J.C., Babała, N., Middendorp, S., van der Horst, G., Xiao, Y., Neves, J.F., Fonseca-Pereira, D., Jacobs, H., Pennington, D.J., et al. (2013). Epithelial and dendritic cells in the thymic medulla promote CD4+Foxp3+ regulatory T cell development via the CD27-CD70 pathway. J. Exp. Med. *210*, 715–728.
56. Konopacki, C., Pritykin, Y., Rubtsov, Y., Leslie, C.S., and Rudensky, A.Y. (2019). Transcription factor Foxp1 regulates Foxp3 chromatin binding and coordinates regulatory T cell function. Nat. Immunol. *20*, 232–242.
57. Stuart, T., Srivastava, A., Madad, S., Lareau, C.A., and Satija, R. (2021). Single-cell chromatin state analysis with Signac. Nat. Methods *18*, 1333–1341.
58. Feng, J., Liu, T., Qin, B., Zhang, Y., and Liu, X.S. (2012). Identifying ChIP-seq enrichment using MACS. Nat. Protoc. *7*, 1728–1740.
59. Korsunsky, I., Millard, N., Fan, J., Slowikowski, K., Zhang, F., Wei, K., Baglaenko, Y., Brenner, M., Loh, P.R., and Raychaudhuri, S. (2019). Fast, sensitive and accurate integration of single-cell data with Harmony. Nat. Methods *16*, 1289–1296.
60. Schep, A.N., Wu, B., Buenrostro, J.D., and Greenleaf, W.J. (2017). chromVAR: inferring transcription-factor-associated accessibility from single-cell epigenomic data. Nat. Methods *14*, 975–978.
61. Kartha, V.K., Duarte, F.M., Hu, Y., Ma, S., Chew, J.G., Lareau, C.A., Earl, A., Burkett, Z.D., Kohlway, A.S., Lebofsky, R., et al. (2022). Functional inference of gene regulation using single-cell multi-omics. Cell Genom. *2*, 100166.
62. Trapnell, C., Cacchiarelli, D., Grimsby, J., Pokharel, P., Li, S., Morse, M., Lennon, N.J., Livak, K.J., Mikkelsen, T.S., and Rinn, J.L. (2014). The dynamics and regulators of cell fate decisions are revealed by pseudotemporal ordering of single cells. Nat. Biotechnol. *32*, 381–386.
63. Bandaranayake, A.D., Correnti, C., Ryu, B.Y., Brault, M., Strong, R.K., and Rawlings, D.J. (2011). Daedalus: a robust, turnkey platform for rapid production of decigram quantities of active recombinant proteins in human cell lines using novel lentiviral vectors. Nucleic Acids Res. *39*, e143.
64. Mirdita, M., Schütze, K., Moriwaki, Y., Heo, L., Ovchinnikov, S., and Steinegger, M. (2022). ColabFold: making protein folding accessible to all. Nat. Methods *19*, 679–682.
65. Goddard, T.D., Huang, C.C., Meng, E.C., Pettersen, E.F., Couch, G.S., Morris, J.H., and Ferrin, T.E. (2018). UCSF ChimeraX: Meeting modern challenges in visualization and analysis. Protein Sci. *27*, 14–25.
66. Nicholson, I.C., Lenton, K.A., Little, D.J., Decorso, T., Lee, F.T., Scott, A.M., Zola, H., and Hohmann, A.W. (1997). Construction and characterisation of a functional CD19 specific single chain Fv fragment for immunotherapy of B lineage leukaemia and lymphoma. Mol. Immunol. *34*, 1157–1165.
67. Yang, J., Baskar, S., Kwong, K.Y., Kennedy, M.G., Wiestner, A., and Rader, C. (2011). Therapeutic potential and challenges of targeting receptor tyrosine kinase ROR1 with monoclonal antibodies in B-cell malignancies. PLoS One *6*, e21018.
68. Davila, M.L., Kloss, C.C., Gunset, G., and Sadelain, M. (2013). CD19 CAR-targeted T cells induce long-term remission and B Cell Aplasia in an immunocompetent mouse model of B cell acute lymphoblastic leukemia. PLoS One *8*, e61338.
69. Paszkiewicz, P.J., Fräßle, S.P., Srivastava, S., Sommermeyer, D., Hudecek, M., Drexler, I., Sadelain, M., Liu, L., Jensen, M.C., Riddell, S.R., et al. (2016). Targeted antibody-mediated depletion of murine CD19 CAR T cells permanently reverses B cell aplasia. J. Clin. Invest. *126*, 4262–4272.
70. Inaba, K., Inaba, M., Romani, N., Aya, H., Deguchi, M., Ikehara, S., Muramatsu, S., and Steinman, R.M. (1992). Generation of large numbers of dendritic cells from mouse bone marrow cultures supplemented with granulocyte/macrophage colony-stimulating factor. J. Exp. Med. *176*, 1693–1702.

71. Bullock, T.N., and Yagita, H. (2005). Induction of CD70 on dendritic cells through CD40 or TLR stimulation contributes to the development of CD8+ T cell responses in the absence of CD4+ T cells. J. Immunol. *174*, 710–717.

72. van der Windt, G.J.W., Chang, C.H., and Pearce, E.L. (2016). Measuring Bioenergetics in T Cells Using a Seahorse Extracellular Flux Analyzer. Curr. Protoc. Immunol. *113*, 3.16B.1–3.16B.14.

73. Hafemeister, C., and Satija, R. (2019). Normalization and variance stabilization of single-cell RNA-seq data using regularized negative binomial regression. Genome Biol. *20*, 296.

74. Hao, Y., Hao, S., Andersen-Nissen, E., Mauck, W.M., 3rd, Zheng, S., Butler, A., Lee, M.J., Wilk, A.J., Darby, C., Zager, M., et al. (2021). Integrated analysis of multimodal single-cell data. Cell *184*, 3573–3587.e29.

STAR★METHODS

KEY RESOURCES TABLE

REAGENT or RESOURCE	SOURCE	IDENTIFIER
Antibodies		
THE™ HIS Tag Antibody – iFluor 647 (1:200)	GenScript	Cat#A01802; RRID: AB_2943644
Brilliant Violet 785 anti-human CD45 (clone HI30, 1:100)	BioLegend	Cat#304031; RRID: AB_10900423
BD Horizon BV421 anti-human CD45RO (clone UCHL1, 1:100)	BD Biosciences	Cat#562641; RRID: AB_2737696
BD Horizon BUV395 anti-human CD45RO (clone UCHL1, 1:40)	BD Biosciences	Cat#564292; RRID: AB_2744410
Alexa Fluor 700 anti-human CD45RA (clone HI100, 1:100)	BioLegend	Cat#304119; RRID: AB_493762
PerCP/Cyanine5.5 anti-human CCR7 (clone G043H7, 1:100)	BioLegend	Cat#353219; RRID: AB_10915275
Brilliant Violet 785 anti-mouse/rat/human CD27 (clone LG3.A10, 1:800)	BioLegend	Cat#124241; RRID: AB_2800595
Brilliant Violet 510 anti-mouse/rat/human CD27 (clone LG3.A10, 1:200)	BioLegend	Cat#124229; RRID: AB_2565795
APC/Cyanine7 anti-human CD27 (clone MT-271, 1:100)	BioLegend	Cat#356423; RRID: AB_2566772
FITC anti-human CD27 (clone O323, 1:100)	BioLegend	Cat#302805; RRID: AB_314297
PerCP/Cyanine5.5 anti-human CD70 (clone 113-16, 1:100)	BioLegend	Cat#355107; RRID: AB_2562478
eFluor 450 anti-human CD69 Monoclonal Antibody (clone FN50, 1:100)	eBioscience	Cat#48-0699-42; RRID: AB_2574025
PE/Cyanine7 anti-human CD137 (clone 4B4-1, 1:100)	BioLegend	Cat#309817; RRID: AB_2287731
BD OptiBuild BUV737 mouse anti-human CD137 (clone 4B4-1, 1:100)	BD Biosciences	Cat#741861; RRID: AB_2871191
APC anti-human CD25 (clone BC96, 1:200)	BioLegend	Cat#302609; RRID: AB_314279
Pacific Blue anti-human CD127 (clone A019D5, 1:50)	BioLegend	Cat#351305; RRID: AB_10718638
Brilliant Violet 605 anti-human CD95 (clone DX2, 1:100)	BioLegend	Cat#305627; RRID: AB_2562444
FITC anti-human CD8α (clone RPA-T8, 1:500)	BioLegend	Cat#301005; RRID: AB_314123
BD Horizon BUV496 mouse anti-human CD8 (clone RPA-T8, 1:500)	BD Biosciences	Cat#612943; RRID: AB_2916884
PE anti-human CD279 (PD-1) Monoclonal Antibody (clone eBioJ105, 1:100)	eBioscience	Cat#12-2799-42; RRID: AB_11042478
PE-Cyanine7 anti-human CD279 (PD-1) Monoclonal Antibody (clone eBioJ105, 1:100)	eBioscience	Cat#25-2799-42; RRID: AB_10853804
BD Horizon PE-CF594 mouse anti-human TIM-3 (clone 7D3, 1:100)	BD Biosciences	Cat#565561; RRID: AB_2744371
Alexa Fluor 647 anti-human TIGIT (clone A15153G, 1:100)	BioLegend	Cat#372723; RRID: AB_2715971
Brilliant Violet 605 anti-human CD223 (LAG-3) (clone 11C3C65, 1:100)	BioLegend	Cat#369324; RRID: AB_2721541
Brilliant Violet 711 anti-human CD39 (clone A1, 1:100)	BioLegend	Cat#328227; RRID: AB_2632893

(*Continued on next page*)

Continued

REAGENT or RESOURCE	SOURCE	IDENTIFIER
PE anti-human EGFR (clone AY13, 1:100)	BioLegend	Cat#352903; RRID: AB_10898161
APC anti-human EGFR (clone AY13, 1:100)	BioLegend	Cat#352905; RRID: AB_11148943
APC-Cyanine7 anti-human CD62L (clone DREG-56, 1:100)	BioLegend	Cat#304813; RRID: AB_493583
FITC anti-human CD19 (clone HIB19, 1:100)	BioLegend	Cat#302205; RRID: AB_314235
PE anti-human CD19 (clone HIB19, 1:100)	BioLegend	Cat#302207; RRID: AB_314237
BD Horizon BV421 anti-human Granzyme B (clone GB11, 1:100)	BD Biosciences	Cat#563389; RRID: AB_2738175
PE mouse anti-TCF-7/TCF-1 (clone S33-966, 1:100)	BD Biosciences	Cat#564217; RRID: AB_2687845
PE mouse IgG1k Isotype Control	BD Biosciences	Cat#554680; RRID: AB_395506
APC anti-human IL-2 (clone MQ1-17H12, 1:100)	eBioscience	Cat#17-7029-82; RRID: AB_469492
PE-Cyanine7 anti-human TNF-α (clone Mab11, 1:100)	BioLegend	Cat#502929; RRID: AB_2204080
PE anti-human IFN gamma (clone 4S.B3, 1:100)	eBioscience	Cat#12-7319-42; RRID: AB_1311247
PE-Cy7 anti-mouse Ki-67 (clone B56, 1:100)	BD Biosciences	Cat#561283; RRID: AB_10716060
PE-Cyanine7 anti-mouse CD39 (clone Duha59, 1:100)	BioLegend	Cat#143805; RRID: AB_2563393
Alexa Fluor 700 anti-mouse CD45.1 (clone A20, 1:200)	BioLegend	Cat#110723; RRID: AB_493732
Brilliant Violet 605 anti-mouse CD279 (PD-1) (clone 29F.1A12, 1:100)	BioLegend	Cat#135219; RRID: AB_11125371
BV711 mouse anti-mouse TIGIT (clone 1G9, 1:100)	BD Biosciences	Cat#744214; RRID: AB_2742063
Brilliant Violet 421 anti-mouse CD366 (TIM-3) (clone RMT3-23, 1:100)	BioLegend	Cat#119723; RRID: AB_2616908
BUV661 anti-mouse CD19 (clone 1D3, 1:200)	BD Biosciences	Cat#612971; RRID: AB_2870243
Brilliant Violet 785 anti-mouse CD223 (LAG-3) (clone C9B7W, 1:100)	BioLegend	Cat#125219; RRID: AB_2566571
BUV395 rat anti-mouse CD8a (clone 53-6.7, 1:500)	BD Biosciences	Cat#565968; RRID: AB_2739421
Pacific Blue rat anti-mouse CD8a (clone 53-6.7, 1:500)	BD Biosciences	Cat#558106; RRID: AB_397029
BUV496 rat anti-mouse CD4 (clone GK1.5, 1:200)	BD Biosciences	Cat#612952; RRID: AB_2813886
PE/Cyanine7 anti-mouse CD70 (clone FR70, 1:300)	BioLegend	Cat#104611; RRID: AB_2750466
FITC anti-mouse CD11c (clone N418, 1:300)	BioLegend	Cat#117305; RRID: AB_313774
BV421 rat anti-mouse I-A/I-E (clone M5/114.15.2, 1:400)	BD Biosciences	Cat#562564; RRID: AB_2716857
APC anti-mouse CD80 (clone 16-10AL, 1:300)	BioLegend	Cat#104713; RRID: AB_313134
Alexa Fluor 700 anti-mouse CD86 (clone GL-1, 1:200)	BioLegend	Cat#105023; RRID: AB_493720
BV711 mouse Anti-Ki-67 (clone B56, 1:100)	BD Biosiences	Cat#563755; RRID: AB_2738406
PE anti-human ERK1/2 phospho [T202,Y204] (clone 6B8B69, 1:30)	BioLegend	Cat#369506; RRID: AB_2629705

(*Continued on next page*)

Continued

REAGENT or RESOURCE	SOURCE	IDENTIFIER
Alexa Fluor 488 anti-human Akt phospho [Thr308] (clone D25E6, 1:50)	Cell Signaling Technology	Cat#43506; RRID: AB_2799244
Alexa Fluor 488 anti-human SHP-1 Rabbit mAb (clone E1U6R, 1:2000)	Cell Signaling Technology	Cat#77181; RRID: AB_2943643
Alexa Fluor 488 Rabbit mAb IgG XP Isotype Control (clone DA1E, 1:1000)	Cell Signaling Technology	Cat#2975; RRID: AB_10699151
Pacific Blue mouse anti-human CD8 (clone RPA-T8, 1:100)	BD Biosciences	Cat#558207; RRID: AB_397058
InVivoMAb anti-mouse CD70	BioXCell	Cat#BE0022; RRID: AB_1107667
InVivoMAb rat IgG2b isotype control	BioXCell	Cat#BE0090; RRID: AB_1107780
TotalSeq™- A0251 anti-human Hashtag 1 Antibody	BioLegend	Cat#394601; RRID: AB_2750015
TotalSeq™- A0252 anti-human Hashtag 2 Antibody	BioLegend	Cat#394603; RRID: AB_2750016
TotalSeq™- A0253 anti-human Hashtag 3 Antibody	BioLegend	Cat#394605; RRID: AB_2750017
TotalSeq™- A0254 anti-human Hashtag 4 Antibody	BioLegend	Cat#394607; RRID: AB_2750018
TotalSeq™- A0255 anti-human Hashtag 5 Antibody	BioLegend	Cat#394609; RRID: AB_2750019
TotalSeq™- A0256 anti-human Hashtag 6 Antibody	BioLegend	Cat#394611; RRID: AB_2750020
TotalSeq™- A0257 anti-human Hashtag 7 Antibody	BioLegend	Cat#394613; RRID: AB_2750021
TotalSeq™- A0258 anti-human Hashtag 8 Antibody	BioLegend	Cat#394615; RRID: AB_2750022
Anti-human CD27 (clone E6S8H) Rabbit mAb	Cell Signaling Technology	Cat#28034; RRID: AB_2943642
Anti-human β2-microgloblulin (clone D8P1H) Rabbit mAb	Cell Signaling Technology	Cat#12851; RRID: AB_2716551
Anti-human β−Actin (clone 13E5) Rabbit mAb	Cell Signaling Technology	Cat#4770; RRID: AB_2223172
Anti-human GAPDH (clone D16H11) XP Rabbit mAb	Cell Signaling Technology	Cat#5174; RRID: AB_10622025
Anti-human TRAF2 (clone C192) Rabbit mAb	Cell Signaling Technology	Cat#4724; RRID: AB_2209845
Anti-human SHP-1 (clone E1U6R) Rabbit mAb	Cell Signaling Technology	Cat#26516; RRID: AB_2934293
Anti-human SHP-1 phospho [Tyr564] (clone D11G5) Rabbit mAb	Cell Signaling Technology	Cat#8849; RRID: AB_11141050
Anti-human SH-PTP-2 (clone B-1) Mouse mAb	Santa Cruz Biotechnology	Cat#sc-7384; RRID: AB_628252
Anti-human SHP1 phospho [Tyr536]	Abcam	Cat#ab41437; RRID: AB_777914
Anti-human SHP1 phospho [Tyr591]	Abcam	Cat#ab41436; RRID: AB_777913
Anti-human Lck (clone D88) XP Rabbit mAb	Cell Signaling Technology	Cat#2984; RRID: AB_2136313
Anti-human phospho Lck [Tyr394] (clone E5L3D) Rabbit mAb	Cell Signaling Technology	Cat#70926; RRID: AB_2924371
Anti-human phospho Lck [Tyr505]	Cell Signaling Technology	Cat#2751; RRID: AB_330446
Anti-mouse IgG, HRP-linked Antibody	Cell Signaling Technology	Cat#7076; RRID: AB_330924
Anti-rabbit IgG, HRP-linked Antibody	Cell Signaling Technology	Cat#7074; RRID: AB_2099233
Bacterial and virus strains		
Turbo Competent *E. coli* (MAX Efficiency DH5α)	Invitrogen	Cat#18258-012

(*Continued on next page*)

Continued

REAGENT or RESOURCE	SOURCE	IDENTIFIER
Biological samples		
Human CD8$^+$ T cells isolated from PBMCs	Fred Hutchinson Cancer Center / Bloodworks Northwest	N/A
Chemicals, peptides, and recombinant proteins		
ES91-17, 100 μM	Sigma-Aldrich	Cat#SML2712; CAS: 55854-43-8
Mdivi-1, 50 μM	Selleck	Cat#S7162; CAS: 338967-87-6
Latrunculin A, 0.04 μM	Sigma-Aldrich	Cat#76343-93-6; CAS: 76343-93-6
Dynasore, see titration	Selleck	Cat#S8047; CAS: 304448-55-3
Dyngo-4a, see titration	Selleck	Cat#S7163; CAS: 1256493-34-1
ULK-101, 5 μM	Selleck	Cat#S8793; CAS: 2443816-45-1
Lactacystin, 20 μM	Tocris	Cat#2267; CAS: 133343-34-7
TPI-1, 0.4 μM	Selleck	Cat#S6570; CAS: 79756-69-7
GM6001, 10 μM	Selleck	Cat#S7157; CAS: 142880-36-2
MitoTracker™ Green, 100 nM	ThermoFisher	Cat#M7514
CellTrace™ CFSE dye, 0.1 μM	ThermoFisher	Cat#C34554
7-AAD	Sigma-Aldrich	Cat#SML1633
Recombinant human IL-2 (clinical grade Proleukin®, Aldesleukin)	Prometheus Laboratories	N/A
Recombinant human IL2	PeproTech	Cat#200-02; GenPept: P60568
Recombinant mouse IL15	PeproTech	Cat#210-15; GenPept: P48346
Recombinant human IL-7	PeproTech	Cat#200-07; GenPept: P13232
Recombinant mouse GM-CSF	PeproTech	Cat#315-03; GenPept: P01587
Ultra-LEAF™ Purified anti-human CD3 (clone OKT3)	BioLegend	Cat#317347 RRID: AB_2571994
Anti-human CD28 (clone TGN1412)	This paper	N/A
Ultra-LEAF™ Purified anti-human CD28 (clone CD28.2)	BioLegend	Cat#302934 RRID: AB_11148949
Anti-human CD70 Dimer Trimer (CD70^{DT})	This paper	N/A
IgG1-Fc	This paper	N/A
Purified NA/LE Hamster Anti-Mouse CD28 (clone 37.51)	BD Pharmingen	Cat#553294 RRID: AB_394763
Purified NA/LE Hamster Anti-Mouse CD3ε (clone 145-2C11)	BD Pharmingen	Cat#553057 RRID: AB_394590
Dynabeads™ Human T-Activator CD3+CD28	Gibco	Cat#11131D
Critical commercial assays		
Chromium Next GEM Single Cell Multiome ATAC + Gene Expression Reagent Bundle	10X Genomics	Cat#1000258
Chromium Next GEM Chip J Single Cell Kit	10X Genomics	Cat#1000230
Chromium Next GEM Chip G Single Cell Kit	10X Genomics	Cat#1000127
CalPhos Mammalian Transfection Kit	Clonetech / Takara	Cat#631312
Seahorse XF Glycolysis Stress Test Kit	Agilent	Cat#103020-100
Seahorse XF Mitochondrial Stress Test Kit	Agilent	Cat#103015-100
P3 Primary Cell 4D-Nucleofector™ X Kit S	Lonza	Cat#V4XP-3032
NucleoSpin RNA XS Micro kit for RNA purification	Macherey-Nagel	Cat#740902
SuperScript IV First-Strand Synthesis System Kit	ThermoFisher	Cat#18091050
EasySep™ Human Naïve CD8+ T Cell Isolation Kit II	STEMCELL	Cat#17968

(*Continued on next page*)

Continued

REAGENT or RESOURCE	SOURCE	IDENTIFIER
EasySep™ Human CD8+ T Cell Isolation Kit	STEMCELL	Cat#17953
EasySep™ Mouse CD8+ T Cell Isolation Kit	STEMCELL	Cat#19853
Pierce™ BCA Protein Assay Kit	ThermoFisher	Cat#23225
Dynabeads™ Protein G Immunoprecipitation Kit	Invitrogen	Cat#10007D
Deposited data		
Multiome Single Cell RNAseq data	This paper	GEO: GSE244834
Experimental models: Cell lines		
Lenti-X™ 293T cells	Clonetech / Takara	Cat#632180 RRID: CVCL_4401
K32	Carl June, Univerisy of Pennsylvania, Maus et al.[19]	N/A
CD70-transgene expressing K32	This paper	N/A
Raji	ATCC	Cat#CCL-86 RRID: CVCL_0511
Raji+ffluc+GFP	This paper	N/A
MDA-MB-231+ffluc+GFP	This paper	N/A
NCI-H1703	ATCC	Cat#CRL-5889 RRID: CVCL_1490
NIH-3T3	ATCC	Cat#CRL-1658 RRID: CVCL_0594
CD40L-transgene expressing NIH-3T3	This paper	N/A
Platinum-E cells	Cell Biolabs Inc.	Cat#RV-101 RRID: CVCL_B488
Experimental models: Organisms/strains		
Mouse: C57BL/6 wildtype (WT)	The Jackson Laboratory	RRID: IMSR_JAX:000664
Mouse: B6.SJL-Ptprca Pepcb/ BoyJ (CD45.1)	The Jackson Laboratory	RRID: IMSR_JAX:002014
Mouse: C57BL/6-Tg(CAG-OVAL)916Jen/J (Act-mOVA)	The Jackson Laboratory	RRID: IMSR_JAX:005145
Mouse: C57BL/6-Tg(TcraTcrb)1100Mjb/ J (OT-1)	The Jackson Laboratory	RRID: IMSR_JAX:003831
Mouse: NOD.Cg-Prkdcscid Il2rgtm1Wjl/ SzJ (NSG)	The Jackson Laboratory	RRID: IMSR_JAX:005557
Oligonucleotides		
sgRNA targeting sequence: SHP-1 (PTPN6): 5' [CAUCCAGCCCACUGAGGUCU] 3''	Synthego	N/A
Primer: PTPN6_Ex2_Forward1: 5' [CTCTCTGCCTGCCCAGACTA] 3'	IDT	N/A
Primer: PTPN6_Ex2_Reverse1: 5' [ACGGGGAACCAGGAATGAGTG] 3'	IDT	N/A
TaqMan Gene Expression Assay: B2M (Hs00187842_m1)	ThermoFisher Scientific	Cat#4331182
TaqMan Gene Expression Assay: *CD27* (Hs00386811_m1)	ThermoFisher Scientific	Cat#4331182
Recombinant DNA		
Lentiviral Packaging Vector: pCHGP-2	This paper	N/A
Lentiviral Packaging Vector: pCMV-Rev2	This paper	N/A
Lentiviral Packaging Vector: pCMV-G	This paper	N/A
Plasmid: epHIV7_hCD19(FMC63) _IgG4_CD28TMD_h41BB_ hCD3ζ_T2A_EGFRt	This paper	N/A
Plasmid: epHIV7_hROR1(R12) _IgG4_CD28TMD_ h41BB_ hCD3ζ_T2A_CD19t	This paper	N/A

(*Continued on next page*)

Continued

REAGENT or RESOURCE	SOURCE	IDENTIFIER
Plasmid: epHIV7_hROR1(R12) _IgG4_CD28TMD_ h41BB_ hCD3ζ_T2A_EGFRt	This paper	N/A
Plasmid: epMP71-mCD19(1D3) _IgG4D28TMD_m41BB_ mCD3ζ_T2A_mCD19t	This paper	N/A
Plasmid: epHIV7_hCD70	This paper	N/A
Plasmid: ep-HIV7_mCD40L	This paper	N/A
Software and algorithms		
FlowJo software v10.8.1	Becton, Dickinson & Company	https://www.flowjo.com/
Thermo TraceFinder 4.1	Thermo Fisher Scientific	https://www.thermofisher.com/us/en/home/industrial/mass-spectrometry/liquid-chromatography-mass-spectrometry-lc-ms/lc-ms-software/lc-ms-data-acquisition-software/tracefinder-software.html
FACSDIVA v9.1	Becton, Dickinson & Company	https://www.bdbiosciences.com/en-us/products/software/instrumentsoftware/bd-facsdiva-software
ID A v2.0 Analysis Software	SONY	N/A
Prism v9.4.0	GraphPad	https://www.graphpad.com/features
Living Image Analysis Software	Perkin Elmer	http://www.perkinelmer.com/product/ li-software-for-spectrum-1-seat-addon-128113
R v4.2.0	CRAN	https://cran.r-project.org/mirrors.html
RStudio v2022.02.3	RStudio	https://rstudio.com/
Cellranger ARC	10X Genomics	https://support.10xgenomics.com/single-cell-multiome-atac-gex/software/downloads
Seurat	Stuart et al.[57]	https://github.com/satijalab/seurat
MACS2	Feng et al.[58]	https://pypi.org/project/MACS2/
Signac	Stuart et al.[57]	https://stuartlab.org/signac/
Harmony	Korsunsky et al.[59]	https://portals.broadinstitute.org/harmony/index.html
ChromVAR	Schep et al.[60]	https://greenleaflab.github.io/chromVAR/index.html
FigR	Kartha et al.[61]	https://buenrostrolab.github.io/FigR/
Monocle3	Trapnell et al.[62]	https://cole-trapnell-lab.github.io/monocle3/
Other		
Trans-blot Turbo System	Bio-Rad	N/A
PVDF membranes	Bio-Rad	Cat#10026934
Mini-PROTEAN® TGX™ Precast Protein Gels	Bio-Rad	Cat#456-1085
ECL Chemiluminescent Substrate	Bio-Rad	Cat#1705062

RESOURCE AVAILABILITY

Lead contact

Further information and requests for resources and reagents should be directed to and will be fulfilled by the lead contact, Stanley R. Riddell (sriddell@fredhutch.org).

Materials availability

Requests for in house synthesized proteins should be directed to the lead contact, Stanley R. Riddell (sriddell@fredhutch.org).

Data and code availability

Multiome-seq data have been deposited at the GEO repository and are publicly available as of the date of publication. Accession number is listed in the key resources table. This paper does not report original code. Any additional information required to reanalyze the data reported in this paper is available from the lead contact upon request.

EXPERIMENTAL MODEL AND STUDY PARTICIPANT DETAILS

Mice

C57BL/6 wildtype (WT), B6.SJL-Ptprca Pepcb/BoyJ (CD45.1), C57BL/6-Tg(CAG-OVAL)916Jen/J (Act-mOVA), C57BL/6-Tg(TcraTcrb)1100Mjb/J (OT-1) and NOD.Cg-Prkdcscid Il2rgtm1Wjl/SzJ (NSG) mice were purchased from Jackson Laboratory and housed in specific-pathogen-free conditions. For all studies, 6-8 week old age-matched and sex-matched male or female mice were used. All mice were housed at the Fred Hutchinson Cancer Center (Seattle, WA). All experiments were performed with the approval of the Institutional Animal Care and Use Committee of the Fred Hutchinson Cancer Center and performed in accordance with institutional and national guidelines and regulations.

Human subjects

Peripheral blood mononuclear cells (PBMCs) were obtained from healthy human donors after written informed consent on research protocols approved by the Institutional Review Board (IRB) of the Fred Hutchinson Cancer Center (Seattle, WA). PBMCs were also purchased from Bloodworks Northwest.

Cell lines

293T Lenti-X cells (Clontech) were cultured in cDMEM (DMEM, 10% FBS, 1 mM L-glutamine, 25 mM Hepes, 100 U/mL penicillin+streptomycin. The K32 cell line was a kind gift from Carl H. June, University of Pennsylvania.[19] K32 cells were cultured in IMDM, 10% FBS and 100 U/mL penicillin+streptomycin. K32 cells were lentiviral transduced with a human truncated CD70 transgene to generate CD70-transgene expressing K32 cells. $CD19^{+}$ Raji lymphoma cells , $ROR1^{+}$ NCI-H1703 lung squamous carcinoma cells and $ROR1^{+}$ MDA-MB-231 triple negative breast cancer cells were purchased from ATCC, lentiviral transduced with a firefly luciferase (ffluc)-expressing transgene and maintained in LCL medium (RPMI 1640, 10% FBS, 1 mM L-glutamine, 100 U/mL penicillin+streptomycin). NIH-3T3 fibroblasts were purchased from ATCC, maintained in cDMEM and lentiviral transduced with a murine CD154 (CD40L)-transgene and used to maturate murine BM derived DCs. Mycoplasma testing was performed bimonthly on all cell lines.

METHOD DETAILS

Recombinant protein design, production and modelling

The $CD70^{DT}$ was constructed with human CD70 (Uniprot: P32970) amino acids Q39-P193. We introduced GS amino acids linking CD70 protomers to generate a single-chain trimer (scT). The designed CD70 scT was fused to human IgG1 Fc (Uniprot: P01857) amino acids E99-K330 with an introduced C103S mutation in the hinge region. The amino acid linker between the CD70 scT and IgG1-Fc was engineered to contain a TEV protease site, 6X Histidine purification tag, and an AviTag. The murine Ig kappa signal peptide was added to the N-terminus of the construct to facilitate secretion. For $CD70^{DT}$ and αCD28 (clone TGN1412) constructs, human codon sequence optimization and gene synthesis was carried out by Genscript. $CD70^{DT}$ and αCD28 (clone TGN1412) were expressed in suspension adapted FreeStyle 293-F cells (ThermoFisher, #R79007) using the Daedalus expression platform as described by Bandaranayake et al.[63] $CD70^{DT}$ and αCD28 (clone TGN1412) were purified from expression culture supernatant by HisTrap FF crude (Cytiva, #11000458) Ni-affinity chromatography or HiTrap MabSelect SuRe (Cytiva, 11003494) protein A affinity chromatography respectively. Following crude affinity purification, proteins were further purified by Superdex 200 (Cytiva, #28-9909-44) size exclusion chromatography. Purified proteins were flash frozen in liquid nitrogen in 1X PBS with 5% glycerol and stored at -80 °C.

The 3D model of $CD70^{DT}$ was generated with ColabFold[64] under default settings using the PDB70 reference database and including Amber side chain relaxation. CD70 scT with the linker region and Fc domains were modeled in Colabfold separately and then joined using ChimeraX[65] to build the full-length model. Pymol (The PyMOL Molecular Graphics System, Version 2.0 Schrödinger, LLC) was used to generate the final images for publication.

CAR construction and virus production

Human CD19- and ROR1-specific CARs were constructed using VL and VH segments of the FMC63[66] and R12[67] mAbs respectively, linked by a human IgG4 spacer domain to a transmembrane domain of human CD28 (UniProt: P10747, aa153-179) and the cytoplasmic domains of human 4-1BB (UniProt: Q07011, aa 214-255) and human CD3ζ (UniProt: P20963, aa52-164). The construct encoded a ribosomal skip element (T2A) and a truncated human epidermal growth factor receptor (EGFRt) or CD19 receptor (CD19t). Transgenes were synthesized and cloned into epHIV7 lentiviral vectors. Lentivirus containing supernatants from 293T cells were produced using packaging vectors pCHGP-2, pCMV-Rev2 and pCMV-G, collected and concentrated prior to cryopreservation.

Mouse CD19-specific CARs were constructed using VL and VH segments of the 1D3[68] mAbs, linked by a mouse IgG4 spacer domain and a transmembrane domain of mouse CD28 (UniProt: P31041, aa151-177) to the cytoplasmic domain of mouse 4-1BB (UniProt: P20334, aa209-256) and mouse CD3ζ (UniProt: P24161, aa52-164). The construct encoded a ribosomal skip element

(T2A) and a truncated human EGF Receptor (EGFRt). Transgenes were synthesized and cloned into pMP71 retroviral vectors and retrovirus containing supernatants were prepared from Platinum-E cells.

T cell isolation, activation and viral transduction

Human $CD8^+$ T cells (bulk and naive) were isolated from PBMC and leukopaks using the EasySep Human $CD8^+$ T cell Isolation Kits (STEMCELL#17968 and STEMCELL#17953) and subsequently cryopreserved. Where indicated, $CD8^+$ Tn, Tcm or Tem cell subsets were FACS-sorted prior to cryopreservation. For all metabolic readouts, freshly isolated or cultured cells were used. For all other experiments T cells were thawed and cultured in RPMI 1640 with 0.02% bovine serum albumin (BSA) for 2 h prior to activation. For activation, T cells were cultured in CTL media (RPMI 1640, 10% human serum, 1 mM L-glutamine, 100 U/mL penicillin+streptomycin, 50 μM β-mercaptoethanol), supplemented with 50 U/mL human IL-2 (Proleukin, Prometheus). Purified T cells were activated for 3 days using plate-bound αCD3 (OKT3, 1-5 μg/ml), αCD28 (TGN1412, 0.2-10 μg/ml), $CD70^{DT}$ (0.8-5 μg/ml) or Human T-Activator CD3+CD28 Dynabeads (BEAD, Thermo Fisher Scientific, 111.31D) at a 3:1 [BEAD:T cell] ratio. Lentiviral transduction of anti-human CD19 CAR (HIV7_FMC63_BBζ_EGFRt), anti-human ROR1 CAR (HIV7_R12_BBζ_CD19t) or anti-human ROR1 CAR (HIV7_R12_BBζ_EGFRt) encoding vectors was performed 24 h after T cell activation. CAR-transduced T cells were expanded for 10 days prior to adoptive transfer.

Mouse T cells were isolated from spleen and lymph nodes using the EasySep Mouse $CD8^+$ T cell Isolation Kit (STEMCELL19853). Purified mouse T cells were activated for 2 days using plate-bound αCD3ε (clone 145-2C11, 1 μg/ml) and αCD28 (clone 37.51, 1 μg/ml) or $CD70^{DT}$ (1 μg/ml) and cultured in mTCM media (RPMI 1640, 10% FBS, 1 mM sodium pyruvate, 1 mM HEPES, 100 U/mL penicillin+streptomycin, 50 μM β-mercaptoethanol), supplemented with 50 U/mL IL2 (PeproTech, #200-02) in the first 3 days and then switched to 50 U/mL IL15 (PeproTech, #210-15) for the following 2 days. Retroviral anti-murine CD19 CAR (MP71_1D3_BBζ_EGFRt) supernatant was spinoculated on retronectin-coated (Takara) plates, before addition and spin transduction of 24 h activated T cells. CAR-transduced T cells were expanded for 5 days prior to adoptive transfer.

Xenograft and B-cell aplasia models

Raji+ffluc lympoma cells ($5x10^5$) were inoculated by intravenous injection (i.v.) into age-matched (6-8 weeks old) NOD/SCID/$\gamma c^{-/-}$ (NSG) male mice. MDA-MB-231+ffluc TNBC cells ($1x10^6$) were inoculated by sub-cutaneous (s.c.) injection into age-matched (6-8 weeks old) NSG male mice. Tumor growth was monitored at weekly intervals using *in vivo* bioluminescence imaging after luciferin administration using the Xenogen IVIS Imaging System (Caliper Life Sciences) and data analyzed using Live Image Software 4.7.2 (Caliper Life Sciences). Seven days after tumor inoculation, $CD8^+$ anti-human CD19 or ROR1 CAR-T cells were injected retro-orbitally (r.o.) at a sub-curative dose of 0.7×10^6 cells per mouse or 8×10^6 cells per mouse. Peripheral blood was drawn weekly to monitor CAR-T cell expansion and further characterization.

B cell aplasia was induced in wildtype C57/BL6 mice by retro-orbital injection of 1×10^6 anti-murine CD19 CAR-T cells derived from splenic $CD8^+$ T cells of CD45.1 congenic wildtype mice. CAR-T cells were administered 4 h after lymphodepletion using 200 mg/kg cyclophosphamide (Cy) administered intraperitoneally (i.p.).[69] B cell aplasia and CAR-T expansion and persistence was monitored weekly in the peripheral blood. Mice were harvested 4 days and 21 days post CAR-T cell infusion for analysis of CAR-T cells in BM and spleen.

Serial restimulation assay

The xCELLigence RTCA eSight (Agilent) platform was used to assess real time impedance-based killing capacity of CAR-T cells. $ROR1^+$ H1703 tumor cells were seeded at a density of $3x10^4$ cells per well in CTL low-dose IL-2 (5 U/mL) and cultured for up to 24 h until cell index of 1-2 was reached. Transduction marker (CD19t) positive anti-human ROR1 (MP71_R12_BBζ_CD19t) CAR-T cells that were expanded for 10 days, purified via positive MACS selection using human CD19 MicroBeads (Miltenyi Biotec, #130-050-301) and added to the target cells at a 1:2 (E:T) ratio in CTL supplemented with IL-2 (5 U/mL). Every other day, CAR-T cells were harvested, MACS-purified and re-plated without E:T ratio adjustment on a newly prepared plate containing $ROR1^+$ H1703 tumor cells. After the 4^{th} re-stimulation round, CAR-T cells were washed and used to assess surface marker expression and cytokine production capacity in response to PMA and ionomycin re-stimulation.

Flow cytometry

Cells were stained in Flow Buffer (PBS, 0.5% FBS, 3.5 μM EDTA) with antibodies to cell-surface markers for 30 min at 4 °C. For intracellular staining, cells were permeabilized for 30 min at room temperature in freshly prepared Perm Buffer (Foxp3 Transcription Factor Fixation kit, eBioscience, #00-5523-00) and incubated for up to 2 h at 4 °C with antibodies specific for cytokines or transcription factors, respectively. To stain for $CD70^{DT}$ binding, THE™-HIS-tag antibody was used. Fixable Viability Dyes were added prior to surface stain in PBS (ThermoFisher; Violet & Aqua; 1:500). Human and mouse reactive antibodies were purchased as specified in the Key Resources Table. Corresponding isotype controls were added where indicated.

For the phospho protein flow, Tn cells were activated in antibody-coated flat-bottom-96-well plates in the presence of DMSO or SHP-1 inhibitor (TPI-1, Selleck, #S6570, 0.4 μM) or actin polymerization inhibitor (LatA, Sigma Aldrich, 0.04 μM). At respective timepoints, cells were immediately fixed using pre-warmed BD™ Cytofix Buffer (BD Pharmingen, #554655) and incubated for 10 min at 37 °C. Cells were then permeabilized in BD™ Phosflow Perm Buffer III (BD Pharmingen, #558050) for 30 min on ice. Subsequently

cells were washed 3 times with Stain Buffer (BD Pharmingen, #554656) and incubated with surface marker, intracellular marker and phospho antibody cocktails for 30 min at RT.

Sample acquisition was performed on a BD Biosciences LSRII Fortessa or Symphony A5 instrument using the FACSDiva software (v9.1; BD Biosciences) or the SONY ID7000™ Spectral Cell Analyzer using the ID A analysis software (v2.0; SONY). Data were analyzed using FlowJo software (v10.8.1; BD Biosciences).

Generation of BM-derived DCs

Murine BM derived DCs were generated as previously described with adaptatioin.[70,71] In brief, BM cells of Act-mOVA mice were harvested and cultured at a density of $2x10^6$ cells per petri dish in R10 mDC medium (RPMI 1640, 10% FBS, 2 mM L-glutamine, 100 U/mL penicillin+streptomycin, 50 μM β-mercaptoethanol), supplemented with 25 ng/mL murine GM-CSF (PeproTech, #315-03). Media change was performed every other day over 10 days. For maturation, DCs were incubated overnight on CD40L-transduced NIH-3T3 fibroblasts at a ratio of 2:1 [DC:3T3]. The morning after, DCs were gently collected from the 3T3 monolayer and characterized by flow cytometry.

Immune co-culture with APCs

K32 or CD70-transgene expressing K32 cells were coated with αCD3 (OKT3, 5 μg/mL) ± αCD28 (TGN1412, 1 μg/mL) mAb for 15 min at 37 °C in RPMI. Following a wash step, αCD3 or αCD3+αCD28-coated K32 cells were co-cultured with human Tn cells at a 1:1 or 5:1 [aAPC:T cell] ratio in a V-bottom 96-well plate in the presence or absence of CME inhibitors (ES9-17 + Mdivi-1). At respective timepoints, cells were subsequently stained following the standard flow or phospho-flow protocols.

Alternatively, $CD8^+$ T cells were isolated from spleens and LNs from OT-1 mice as described above. T cells were then co-cultured with BM derived Act-mOVA DCs at a [1:1] ratio in the presence of blocking FR70 or IgG antibody (20 μg/mL). At indicated timepoints, T cells were washed, Fc-block was added, and surface staining was performed.

Internalization and cleavage assay

Prior to activation, T cells were pre-incubated in RPMI 0.02% for 10 min at 37 °C with Dynasore (Selleck, #S8047, titration), Dyngo-4a (Selleck, #S7163, titration), ES9-17 (Sigma-Aldrich, #SML2712, 100 μM) and/or M-divi1 (Selleck, #S7162, 50 μM) to inhibit CME. Latrunculin A (Sigma Aldrich, #L5163, 0.04 μM) was added at the time of activation. GM6001 (Selleck, #S7157, 10 μM) was used to inhibit CD27 cleavage. T cells were seeded at a density of $1x10^5$ cells per 96-well to the antibody-coated flat-bottom plates and centrifuged for 1 min at 400 x g. At indicated timepoints of activation, cells were removed from the activation plate, transferred to a new 96-U-bottom-well plate on ice and subsequently stained for surface marker expression at 4 °C for 30 min before analysis by flow cytometry.

Protein degradation assay

Prior to activation, T cells were pre-incubated with inhibitors in RPMI 0.02% for 10 min at 37 °C. The following inhibitors were used: ES9-17 (Sigma-Aldrich, #SML2712, 100 μM), Mdivi-1 (Selleck, # S7162, 50 μM), ULK-101 (Selleck, #S8793, 5 μM), Lactacystin (Tocris, #2267, 20 μM). T cells were seeded at a density of $1x10^5$ cells per 96-well to the antibody-coated flat-bottom plates and immediately centrifuged for 1 min at 400 x g. After 10 min of activation, pre-warmed Cytofix Buffer (BD, #554655) was added to wells and incubated for additional 10 min at 37 °C. Cells were then transferred to a 96-U-bottom-well plate and permeabilized with freshly prepared Cytofix+Cytoperm solution of the FOXP3 staining kit (eBioscience, #00-5523-00) for 30 min at RT. Cells were washed in freshly prepared 1X PermBuffer (eBioscience, #00-5523-00) and stained for 2 h in 1X PermBuffer containing antibodies. Total cellular protein expression was assessed by flow cytometry.

Metabolic assays

To evaluate mitochondrial mass, cultured cells were washed in pre-warmed PBS and stained with Mitotracker Green (ThermoFisher, Cat#M7514, 100 nM) and surface marker antibodies for 15 min at 37 °C. Cells were washed with pre-warmed CTL medium and subsequently analyzed by flow cytometry. Seahorse assays were performed as described.[72] Rehydrated Seahorse XF cartridges were incubated in XF calibrant for 1 h at 37 °C (no CO_2) prior to starting the experiment. Human T cells (5 or 10 days post activation) were counted and the concentration was adjusted to $5x10^6$ cell per mL in complete RPMI XF assay media (Agilent, Cat#103015-100). This media was supplemented with additional substrates for the Mito Stress Test (2 mM L-Glutamine, 1 mM Pyruvate, 10 mM Glucose, 50 U/mL IL2) and for the Glucose Stress Test (2 mM L-Glutamine, 50 U/mL IL2). T cells were added to plates coated with poly-L-lysine (Sigma Aldrich, Cat#P8920,100 μg/mL) at a density of $2x10^5$ cells per well and centrifuged for 5 min at 400 x g to adhere the cells to the plate. Metabolic profiles were assessed by injection of oligomycin (1.5 μM), carbonyl cyanide-4-(trifluoromethoxy) phenylhydrazone (FCCP, 0.5 μM), rotenone (0.5 μM), antimycin A (0.5 μM), glucose (10 mM), 2-deoxyglucose (2-DG, 50 mM). Data were generated using XF report generator software (Agilent).

Proliferation and cell cycle analysis

Tn cells were resuspended in pre-warmed PBS containing 0.1 μM CellTrace™ carboxyfluorescein succinimidyl ester (CFSE) dye (ThermoFisher) and labelled for 10 min in a 37 °C waterbath and vortexed at half-time. Labelling was quenched with FBS and T cells were washed 3 more times with pre-warmed CTL medium. Tn cells were activated in antibody-coated or BEAD containing

flat-bottom-96-well plates (non-tissue culture treated) at a density of 10^5 cells per well in CTL + 50 U/mL IL-2. CFSE dilution was assessed by flow cytometry 72 h post Tn cell activation.

Cell cycle analysis was performed 48 h and 96 h post Tn cell activation. Cultured cells were washed in PBS and stained with surface antibodies in FACS buffer for 30 min at 4 °C. Cells were then permeabilized in ice-cold 70% ethanol and kept on ice for 1 h. After two consecutive wash steps, cells were stained in PFT buffer (PBS, 1% FBS, 0.25% Triton X-100) containing 25 mg/mL 7-aminoactinomycin D (7-AAD; Sigma-Aldrich) for 30 min at RT in the dark. Cells were washed twice in FACS buffer and analyzed by flow cytometry.

Glucose tracing

Tn cells were harvested from donors and plated at $4x10^5$ cells per 100 μl well of a pre-coated 96-well dish. Cells were grown in glucose free RPMI (Gibco, #11979020) supplemented with 10% dialyzed human serum, 1mM L-glutamine, 100 U/mL penicillin+ streptomycin, 50 μM β-mercaptoethanol and 100 μM [1,2-^{13}C] Glucose (Cambridge Isotopes, CLM-504-PK). The supernatant was collected at the indicated time points, centrifuged, and frozen until extraction. Metabolites were extracted from 20 μl of each sample with 300 μL of 100% HPLC grade ethanol, centrifuged (17,000 x g, 10 min, 4 °C), moved to new Eppendorf tubes, lyophilized, and stored at 20 °C. Lyophilized samples were then resuspended in 80% HPLC grade methanol and HPLC grade water.

LC-MS metabolite quantification

Metabolite extracts were analyzed on a QExactive HF-X hybrid-Orbitrap mass spectrometer equipped with an Ion Max API source and HESI-II probe, coupled to a Vanquish Flex Binary UHPLC system (Thermo Scientific, Waltham, MA). A 1 μL sample injection was gradient eluted from a Millipore 2.1x150 mm (5 μm particle size) ZIC-pHILIC column (Millipore, Burlington, MA) using a mobile phase gradient as follows: 0-20 min: 85-20% "B", followed by a hold at 20% "B" for 4 min, followed by a return to 85% "B" over 0.5 min, and finishing with a column re-equilibration at 85% "B" for 10 column volumes. The flow rate was at 150 μL/min, the autosampler compartment temperature was set to 10 °C, and the column temperature used was 30 °C. Mobile phase "A" consisted of 20 mM ammonium carbonate and 0.1% ammonium hydroxide (v:v), while mobile phase "B" consisted of 100% acetonitrile.

Metabolites were detected over a range of 70-1050 m/z in the MS1 full-scan mode in both positive and negative polarities. Data were collected in the profile mode at 240K resolution (@ 200 m/z) using an AGC target value of 3,000,000 and a maximum injection time of 250 msec, with a chromatographic peak width (FWHM) set at 10 sec. The source parameters used with the HESI probe were as follows: sheath and aux gas flow rates at 40 and 20 units respectively, spray voltage of 2.5 kV, a capillary temperature of 335 °C, and the aux. gas heater temperature was 350 °C. The ion funnel level was set at 40%.

Gene deletion in resting human Tn cells

Tn cells were freshly isolated from PBMCs as described above. To form the CRISPR-Cas9-sgRNA RNP complex, synthetic SHP-1 sgRNAs (Synthego) were incubated with Cas9 nuclease protein NLS (Horizon Discovery, Cat# CAS12206) at a ratio of [4:1] (160 pmol sgRNA+ 40 pmol Cas9) for 15 min at 37 °C and then kept at 4 °C until further processed. Per single reaction, $2x10^6$ freshly isolated Tn cells were washed twice with pre-warmed PBS and resuspended in 20 μl of P3 buffer (Lonza, V4XP-3032). The RNPs where then mixed with the cell 20 μl of cell suspension and transferred into a 16-well reaction cuvette of the 4D-Nucleofector System (Lonza). Cells were nucleofected using program EH-100 on the 4D-Nucleofector system. Immediately after electroporation, 80 μl of pre-warmed complete T cell media (CTL) containing 0.5 ng/mL human IL-7 (PeproTech, 200-07) was added to each well in the cuvette and incubated for 15 min at 37 °C for recovery. A total of 100 μL cell suspension was then gently transferred into individual 48-wells and supplemented with 800 μL of CTL containing human IL-7. Half-media change was performed every other day which allowed resting Tn cells to maintained over a culture period of 8 days. SHP-1 knock-out efficiencies were assessed using intracellular staining for SHP-1 following the ERK1/2 phos-flow staining protocol and sanger sequencing (https://ice.synthego.com/#/analyze/results/nyhutj3v19gvwksh). For functional experiments SHP-1 sgRNA #8 was selected. Sequence of sgRNA #8 as well as sequencing primer pairs are provided in the key resources table.

Single-cell RNA and ATAC sequencing

Cryopreserved Tn cells from n = 1 donor (previously processed as described above) were thawed and activated for 24 h with either αCD3+αCD28 BEADs at a 3:1 [BEAD:T cell] ratio or with combinations of plate-bound αCD3 (5 μg/mL), αCD28 (0.2 μg/mL) and $CD70^{DT}$ (0.8 or 5 μg/mL). Additionally, Tn cells from the same donor were thawed and directly readied for nuclei isolation without activation. To minimize batch effects, cells from each stimulation condition were captured in a single lane using 10x Genomics multiome chemistry. Prior to capture, cells were hashed using TotalSeq™-A HTO anti-ubiquitous cell-surface-epitope DNA-barcoded antibodies (BioLegend, see key resources table), according to manufacturer's protocol. The "hash-tagged" cells underwent a gentle fixation by incubation at room temperature in 1X PBS 0.1% formaldehyde for 10 min, then quenching with glycine at 0.125 M and immediately washing with ice cold 1X PBS (supernatant removed by spinning cells at 500 × g for 5 min). Next, nuclei preparation was performed according to manufacturer's specification (document # CG000356 Rev B), with the following optimization step. The optimal permeabilization and lysis time was determined by incubating the samples into 100 μL chilled lysis buffer for 2, 3, 4, 5, or 6 min on ice, then proceeding to the washing step. The quality of obtained nuclei was assessed using Acridine Orange and Propidium Iodide staining (Nexcelom Viastain AOPI # CS2-0106-25 mL) as well as visualizing cell morphology under a microscope. The

"2 min" mark was determined as the optimal permeabilization time with cell viability of 89-97% and cell integrity maintained as viewed under the microscope. After cell counting, equal numbers of nuclei from the samples were pooled to a single tube in 1X Diluted Nuclei Buffer (10x Genomics, PN-2000207) at ~3,500 nuclei per μL. The nuclei were then prepared for transposition according to the 10x Genomics Next GEM Single Cell Multiome ATAC + Gene Expression User Guide (document # CG000338 Rev D). Ten thousand nuclei were targeted for capture. Libraries were sequenced using an Illumina NextSeq 2000. 7862 and 11063 cells were included post quality control for downstream final analysis of the respective experiment.

Single-cell RNA and ATAC computational analysis

Illumina BCL files were demultiplexed and processed using cellranger ARC. ATAC peaks were called on the resulting fragments file using MACS2[58] with the parameters '—nomodel –extsize 200 –shift -100'. RNA counts and fragment reads in MACS2 peaks matrices were counted using Signac.[57] Cells meeting the following thresholds were retained for downstream analysis: percent mitochondrial RNA reads < 15%; 3 < $\log_{10}$(ATAC counts) < 5; 3 < $\log_{10}$(RNA/UMI counts) < 4.5; Fraction of reads in peaks > 40%; nucleosome_signal < 1.5; TSS.enrichment > 1. RNA counts were normalized using SCT transform[73] prior to PCA dimensionality reduction, after which batch correction was performed using Harmony.[59] ATAC counts underwent TFIDF/SVD[57] dimensionality reduction. An integrated UMAP embedding was created using the FindMultiModalNeighbors[74] function. Cell subtypes were classified using the standard Seurat workflow. Cis-regulatory elements were identified with the 'LinkPeaks' function and motif deviation scores were computed using ChromVAR.[60] Target genes of highly utilized transcription factors were inferred and calculated using FigR.[61] Pseudotime trajectory analysis was performed using the PlotGenesInPseudotime function in Monocle3.[62]

Western blot assay

5x10^5 non-activated or plate-activated bulk $CD8^+$ or Tn cells were transferred to an Eppendorf tube and washed with ice-cold PBS. Cell pellets were then resuspended in ice-cold NP-40 lysis buffer (Invitrogen, #FNN0021) supplemented with protease inhibitor and phosphatase inhibitors (Thermo Scientific, #78430 and #78428). Lysates were vigorously vortexed and kept on ice for additional 10 min to allow complete lysis. Lysates were centrifuged for 15 min at 16000 x g and lysates subsequently transferred to new Eppendorf tubes. Protein concentrations were quantified using Pierce™ BCA Protein Assay Kit (Thermo Scientific, #23225). 4X Laemmli Sample buffer (Bio-Rad, #1610747) and NuPAGE Sample Reducing Agent (Invitrogen, # NP0009) were added to the protein lysate prior to denaturation at 95 °C for 5 min.

Gel electrophoresis was performed using Mini-PROTEAN® TGX™ Precast Protein Gels (Bio-Rad, #456-1085) in freshly prepared Tris+Glycine+SDS Running Buffer (Bio-Rad, #1610732). Transfer to PVDF membranes (Bio-Rad, #10026934) was performed in transfer buffer (Bio-Rad, #10026938) using Trans-blot Turbo System (Bio-Rad). For membrane blocking and antibody incubation blocking buffer (Bio-Rad, #12010020) was used. Membranes were incubated over night at 4 °C with primary antibodies listed in the key resources table. Membranes were incubated with secondary HRP-linked antibodies for 1 h at room temperature. Membranes were incubated with ECL Chemiluminescent Substrate (Bio-Rad, #1705062) and developed using the iBright FL1000 gel imaging system (Invitrogen).

Immunoprecipitation assay

3-5x10^6 non-activated or plate-activated Tn cells were transferred to Eppendorf tube and washed with ice-cold PBS. Sample preparation was performed as described for western blot analysis. Lysates were kept on ice while Dynabeads Protein G (ThermoFisher, #10003D) were conjugated with antibody. 50 μl Dynabeads per reaction were transferred to an Eppendorf tube, washed with PBS and magnetized 3 times for 5 min. TRAF2 antibody (Cell Signaling, #4724) and SHP-1 antibody (Cell Signaling, #26516), were incubated with the Dynabeads for 1 h at RT under rotation. Dynabeads were then magnetized for 5 min and washed with PBS-Tween (0.02%) for 3 min 5 times. Dynabeads were then resuspended in freshly prepared 5 mM BS3 (ThermoFisher, #A39266) cross-linker solution and incubated for 30 min under rotation. Subsequently, cross-linking reaction was quenched adding 1 M Tris-buffer to the Dynabead cross-linking solution at a final concentration of 35 mM. Dynabeads were magnetized for 5 min and washed 3 more times for 5 min. Cell lysates were now added to antibody-conjugated Dynabeads and kept under rotation overnight at 4 °C. After overnight incubation, Dynabeads were magnetized and un-bound supernatant fractions discarded. Antibody-captured proteins were eluted from Dynabeads in elution buffer consistent of Laemmli Sample Buffer (Bio-Rad, #1610747) and NuPAGE Sample Reducing Agent (Invitrogen, # NP0009) and boiled at 95 °C for 5 min. Gel electrophoresis and transfer were performed as described for Western Blot analysis.

Quantitative PCR

RNA was extracted using the NucleoSpin RNA XS Micro kit for RNA purification (Macherey-Nagel, # 740902.50) and cDNA synthesized using the SuperScript IV First-Strand Synthesis System kit (ThermoFisher, #18091050). Amplifications were performed for 45 cycles on a Quant Studio 5 Real-Time PCR system in a 10 μl reaction consisting of 2X TaqMan™ Universal Master Mix with UNG (Applied Biosystems, #4440046), 2-5 ng of cDNA, and 20X TaqMan™ Gene Expression Assay probes (Applied Biosystems): *B2M* (Hs00187842_m1), *CD27* (Hs00386811_m1). The cycle threshold (Ct) was determined using QuantStudio Analysis Software, normalized to housekeeping gene *B2M*, and the level of gene expression calculated using the comparative Ct method (2(^Ct)). Log-2 fold-change (FC) was calculated between activated and non-activated T cell groups.

QUANTIFICATION AND STATISTICAL ANALYSIS

Statistical analysis

All data are represented as the mean values ± SEM. Statistical significance was determined by paired and unpaired two-tailed Student's t-test, one-way ANOVA, tow-way ANOVA, Log-Rank (Mantel-Cox) test and Turkeys multiple comparison test as indicated in the figure legends using Prism software (GraphPad). Statistical significance was established at the levels of * $p<0.05$; ** $p<0.01$; *** $p<0.005$; **** $p<0.001$.